

**FORMATION OF RELATIVISTIC OUTFLOWS IN
SHEARING BLACK HOLE ACCRETION CORONAE**

Prasad Subramanian¹, Peter A. Becker²

Center for Earth Observing and Space Research,
Institute for Computational Sciences and Informatics,
George Mason University, Fairfax, VA 22030-4444

¹ *also* Code 7660, Naval Research Laboratory,
Washington, DC 20375, psubrama@mahanadi.nrl.navy.mil

² *also* Department of Physics and Astronomy,
George Mason University, Fairfax, VA 22030-4444, pbecker@gmu.edu

Demosthenes Kazanas

Laboratory for High-Energy Astrophysics,
NASA/Goddard Space Flight Center, Greenbelt, MD 20771,
kazanas@milkyway.gsfc.nasa.gov

Received _____; accepted _____

accepted for publication in the *Astrophysical Journal*

ABSTRACT

We examine the possibility that the relativistic jets observed in many active galactic nuclei may be powered by the Fermi acceleration of protons in a tenuous corona above a two-temperature accretion disk. In this picture the acceleration arises as a consequence of the shearing motion of the magnetic field in the corona, which is anchored in the underlying Keplerian disk. The protons in the corona have a power-law distribution because the density there is too low for proton-proton collisions to thermalize the energy supplied via Fermi acceleration. The same shear acceleration mechanism also operates in the disk itself, however, there the density is high enough for thermalization to occur and consequently the disk protons have a Maxwellian distribution.

Particle acceleration in the corona leads to the development of a pressure-driven wind that passes through a critical point and subsequently transforms into a relativistic jet at large distances from the black hole. We combine the critical conditions for the wind with the structure equations for the disk and the corona to obtain a coupled disk/corona/wind model. Using the coupled model we compute the asymptotic Lorentz factor Γ_∞ of the jet as a function of the cylindrical starting radius at the base of the outflow, in the corona. Our results suggest that $\Gamma_\infty \lesssim 10$, which is consistent with observations of superluminal motion in blazars. We show that collisions between the jet and broad-line emission clouds can produce high-energy radiation with a luminosity sufficient to power the γ -rays observed from blazars.

Subject headings: radiation mechanisms: non-thermal, accretion, accretion disks, acceleration of particles, gamma rays: theory

1. INTRODUCTION

Jets are among the most ubiquitous of astrophysical phenomenon, and are associated with objects ranging from protostars and binary systems in our galaxy to supermassive black holes in the centers of Active Galactic Nuclei (AGNs). Large asymptotic Lorentz factors are implied by observations of superluminal motion in many blazars (Dermer & Schlickeiser 1992; Vermeulen & Cohen 1994), and the *EGRET* instrument on board the *Compton Gamma-Ray Observatory* (*CGRO*) has also detected intense γ -ray flares from many of these sources (Wehrle et al. 1998). The mechanisms responsible for producing the observed jets are still poorly understood, but collimated outflows in general appear to be associated with objects that derive their luminosity from the accretion of matter onto a gravitating object (e.g., Dermer & Schlickeiser 1992). The asymptotic jet velocity observed far from the central object is probably related to the depth of the gravitational potential at the radius of jet formation. The observations of relativistic jets with asymptotic Lorentz factors $\Gamma_\infty \lesssim 10$ suggest an origin relatively close to the black hole horizon, implying the existence of extreme conditions at the base of the outflow. Despite the overall consensus that AGNs presumably contain accretion disks, little, if any, connection has been established between the observed jets and the underlying disks. Our goal in this paper is to explore the possibility that the energy responsible for powering the jets is transferred to the jet particles via a second-order Fermi acceleration mechanism driven by the shear of the accretion disk.

There has been a significant amount of recent interest in interpreting the observed high-energy emission from blazars as arising from hadronic jets (e.g., Mannheim 1993; Dar & Laor 1997), and a variety of different mechanisms have been proposed to channel the required energy from the protons into the γ -rays. A complete theoretical understanding of the emission mechanisms operating in these sources is going to be particularly important for the interpretation of the wealth of data expected from the upcoming *GLAST* observations of AGNs. It seems clear that while the X-ray and soft γ -ray ($\lesssim 10$ MeV) components of typical AGN spectra can be successfully attributed to leptonic models, the GeV and TeV emission are better explained by hadronic models, involving either proton-induced cascades (Mannheim 1993) or collisions between the hadronic jet and target

protons located in the broad-line emission region (Dar & Laor 1997). One of the reasons hadronic models are better suited to explain the GeV and TeV emission is that hadrons do not suffer from the severe radiative losses associated with electrons, and therefore hadrons do not require large in situ reacceleration rates. Furthermore, GeV energies emerge as natural scales in hadronic processes such as the strong proton-proton interaction. However, the origin of the energetic hadrons in the jets is ambiguous. Most models utilizing protons beams make the ad hoc assumption that the protons are acceleration by shocks running up and down the jet. While shock acceleration might very well be taking place, the connection between the jet and the underlying accretion disk which surrounds the central object still remains unclear.

In principle, radiation pressure provides another means for accelerating the gas, but this mechanism alone probably cannot power a highly relativistic outflow regardless of whether it is optically thin or thick. Under optically thin conditions, the aberration of the background photons will cause them to approach from the head-on direction in the frame of the outflowing gas, impeding rather than accelerating a relativistic outflow (Phinney 1982). Conversely, under optically thick conditions the photon energy density at the base of the flow must exceed the rest mass energy density by at least one order of magnitude in order to achieve an asymptotic Lorentz factor $\Gamma_\infty \sim 10$ (cf. Mészáros & Rees 1992). This probably cannot occur in the accretion disk, where we expect rough equipartition between the matter and the radiation.

Magnetocentrifugal acceleration may provide another mechanism for producing relativistic jets (Blandford & Payne 1982; Contopoulos & Lovelace 1994; Contopoulos 1995). In this scenario, energy associated with the rotation of a cold accretion disk is transferred via magnetic stresses to the tenuous gas in an overlying corona, resulting in the acceleration of the gas to relativistic speeds in a magnetically confined jet (Li, Chiueh, & Begelman 1992). Most theoretical treatments of magnetocentrifugal acceleration make drastic simplifications, such as assuming self-similar dependences of the flow parameters on the radial distance. These treatments require the poloidal magnetic field at the disk surface to be inclined at a sufficiently large angle away from the z -axis in order for the acceleration mechanism to be effective. The simulations of Ustyugova et al. (1995) suggest that the asymptotic flow velocities attained via the magnetocentrifugal acceleration

mechanism are only mildly relativistic at best. Furthermore, the stability of these magnetically confined flows is uncertain (Begelman 1998), and it is unclear how the existence of the relativistic outflow is related to the values of the macroscopic physical parameters in the underlying accretion flow.

Hydrodynamical acceleration driven by the pressure of the hot gas itself provides a third mechanism for the production of relativistic outflows. This has been proposed by Mastichiadis & Kazanas (1993) and developed in greater detail by Contopoulos & Kazanas (1995). In these models the required heating of the gas is accomplished in situ via shocks or turbulence (Protheroe & Kazanas 1983; Kazanas & Ellison 1986), and the outflow may also receive additional power from the decay of relativistic neutrons throughout the jet. Within the context of this general scenario, the thickness of the accretion disk divided by the neutron flight distance determines whether highly relativistic outflows are possible in a given situation (Contopoulos & Kazanas 1995). However, in general, these “distributed power” models lack a detailed connection with the physics of the underlying accretion disk.

In the present paper we examine a new type of disk/jet connection by considering a simple model for the production of a relativistic outflow based on the hydrodynamical expansion of a gas which is heated via a Fermi acceleration mechanism. This is dynamically similar to the distributed-power models except that the heating takes place at the base of the outflow only, where it is possible to establish a direct connection between the required proton acceleration and the properties of the accretion disk. The outflowing gas must have positive energy in order to escape from the black hole, so that the resulting wind is super-virial (e.g., Blandford & Begelman 1999). Romanova et al. (1998) performed numerical simulations of the dynamics of magnetic loop configurations in the coronae of accretion disks. They found that the loops open up due to differential rotation in the disk, leading to transient outflows driven by pressure from toroidal magnetic fields.

In the model considered here the energy is also supplied via differential rotation in the disk, but the specific mechanism involved is second-order Fermi acceleration occurring in the tenuous corona due to the motion of magnetic field lines anchored in the disk. Microphysically, the Fermi acceleration results from collisions between seed (thermal) protons and magnetic scattering centers

(“kinks”) whose motion is driven by the Keplerian shear flow of the underlying disk. In this model, the magnetic field produces a viscous torque on the disk, and the dissipated azimuthal kinetic energy is transferred to the corona primarily by the Poynting flux of the shearing field rather than by the thermal protons diffusing up from the disk. We show that this process results in a relativistic power-law tail in the coronal proton distribution, with enough pressure to drive the particles out of the corona as a transonic electron-proton wind. Beyond the sonic (critical) point, the wind transitions into a relativistic outflow with an asymptotic bulk Lorentz factor $\Gamma_\infty \sim 3 - 10$. The scenario of protons interacting with the tangled magnetic field has been considered by Subramanian, Becker, & Kafatos (1996, hereafter Paper I) as one of the mechanisms responsible for providing the viscosity in the accretion disk. Hence the same physical process which accomplishes the transfer of angular momentum in the disk also produces the acceleration of the relativistic protons in the corona.

The remainder of the paper is organized as follows. In § 2 we present a detailed analysis of the correspondence between the viscosity mechanism introduced in Paper I and the second-order Fermi acceleration mechanism considered in this paper. After we have established the equivalence of the two scenarios, we focus in § 3 on solution of the steady-state transport equation describing the energy distribution of the protons accelerated in the corona. In § 4 we develop the formalism required to self-consistently link the corona with the underlying disk, resulting in a coupled disk-corona model. The details of the wind/jet formation process are considered in § 5, and in § 6 we discuss the model self-consistency requirements. Computational results obtained using the fully coupled disk/corona/wind model are presented in § 7, and in § 8 we conclude with a discussion of our results and the associated implications for γ -ray observations of blazars.

2. FERMI ACCELERATION AND VISCOSITY

We begin by investigating the connection between the viscosity mechanism discussed in Paper I and the Fermi acceleration scenario considered in this paper by comparing the heating rates associated with the two processes. As in Paper 1, we will focus on hot, two-temperature accretion disks with ion (proton) temperatures $T_i \sim 10^{12}$ K and electron temperatures $T_e \sim 10^9$ K.

We are mainly concerned here with the energetic consequences of collisions between hot protons and kinks in the magnetic field that are participating in the shear flow of the Keplerian disk. In order to focus on the direct effects of the magnetic shear, we assume that the kinks are “cold,” meaning that they have no stochastic motion. The validity of this assumption will be investigated later when we consider the consequences of replacing the cold kinks with propagating, stochastic MHD waves. Although our specific application involves the acceleration of protons in a corona overlying the disk, our discussion of the shear acceleration mechanism will remain general at this point.

2.1. *Fermi Acceleration in Shear Flows*

A qualitative argument for the second-order nature of the Fermi acceleration mechanism operating in a shear flow can be constructed as follows. Consider a proton originating in the (stationary) middle layer in Figure 1 and experiencing a subsequent collision with a scattering center (cold magnetic field kink) located in Quadrant 2. Since this is an approaching collision, the proton will gain energy. Conversely, the corresponding collision in Quadrant 1 is an overtaking one, and therefore the proton will lose energy in this case. Following this chain of logic for the other two quadrants, we conclude that to first order in the relative shear velocity between successive scattering centers, Δv , there is no mean gain or loss of energy for the incident proton. However, the approaching collisions take place on a shorter timescale than the overtaking ones, and therefore, to second order in Δv , acceleration dominates over deceleration.

The theoretical basis for second-order Fermi acceleration due to collisions with scattering centers embedded in a shear flow has been examined in the context of cosmic ray energization by Earl, Jokipii, & Morfill (1988) and by Webb, Jokipii, & Morfill (1994), and the application to accretion flows has been discussed by Katz (1991). Typically, second-order Fermi acceleration occurs when particles interact with randomly-moving scattering centers, whereas the interaction of particles with systematically-moving scattering centers (e.g. in a converging flow) usually results in first-order Fermi acceleration. In our situation, the scattering centers (kinks in the tangled magnetic field) are embedded in a systematic (Keplerian) flow, and are cold (no stochastic motion).

Nonetheless, as discussed above, the interaction results in a mean fractional energy gain per scattering $\Delta\epsilon/\epsilon \propto \Delta v^2$, where ϵ is the proton energy. The acceleration mechanism considered here is therefore hybrid in nature since it is a *second-order* process operating in a *systematic* background flow.

When the scattering centers are contained in a Keplerian shear flow, the mean fractional energy gain per scattering is given by

$$\frac{\Delta\epsilon}{\epsilon} \sim \left(\frac{\Delta v_\phi}{c}\right)^2 = \left(\frac{\tilde{\lambda}}{c} \frac{dv_\phi}{dR}\right)^2, \quad (2.1)$$

where $\tilde{\lambda}$ is the mean free path for collisions between protons and magnetic scattering centers, c is the speed of light, v_ϕ denotes the Keplerian orbital velocity, and $\Delta v_\phi \equiv \tilde{\lambda}(dv_\phi/dR)$ gives the characteristic relative shear velocity between successive scattering centers. In this type of situation, we can model the diffusion of the protons in energy space using a simple transport equation of the form

$$\frac{\partial f}{\partial t} = -\frac{1}{\epsilon^2} \frac{\partial}{\partial \epsilon} \left(-\epsilon^2 \mathcal{D} \frac{\partial f}{\partial \epsilon} \right), \quad (2.2)$$

where \mathcal{D} is the energy diffusion coefficient and the distribution function f is related to the ion number density N and energy density U by

$$N = \int_{m_p c^2}^{\infty} \epsilon^2 f d\epsilon \sim \text{cm}^{-3}, \quad (2.3)$$

$$U = \int_{m_p c^2}^{\infty} \epsilon^3 f d\epsilon \sim \text{ergs cm}^{-3}, \quad (2.4)$$

with m_p denoting the proton mass. Note that equation (2.2) considers only diffusion in energy space, and ignores spatial transport. We will have occasion later in the paper to replace the lower bound of integrals like those in equations (2.3) and (2.4) with zero, because the mathematical structure of the relevant equations will allow for the diffusion of particles to negligibly small energies. We will not, however, be making a serious error by adopting a lower bound of zero in such situations, because we will be dealing with relativistic proton distributions containing very few particles with energies close to $m_p c^2$.

2.2. Energy Diffusion Coefficient

We can quantify the energy diffusion coefficient \mathcal{D} introduced in equation (2.2) by relating it to the fractional energy change per scattering given by equation (2.1). Using equation (A2), we express the mean energization rate due to shear acceleration for protons with energy ϵ as

$$\langle \dot{\epsilon}_{\text{shear}} \rangle = \frac{1}{\epsilon^2} \frac{d}{d\epsilon} (\epsilon^2 \mathcal{D}) = 4 \epsilon D, \quad (2.5)$$

where we have adopted the form for the energy diffusion coefficient

$$\mathcal{D}(\epsilon) = D \epsilon^2 \sim \text{ergs}^2 \text{ s}^{-1} \quad (2.6)$$

with $D = \text{constant}$, which is appropriate for cases involving an energy-independent magnetic scattering cross section. Note that $\langle \dot{\epsilon}_{\text{shear}} \rangle \propto \epsilon$, as is typical of Fermi processes. We can write another expression for the acceleration rate based directly on equation (2.1), which yields

$$\frac{\Delta \epsilon}{\Delta t} = \epsilon \left(\frac{\tilde{\lambda}}{c} \right) \left(\frac{dv_\phi}{dR} \right)^2, \quad (2.7)$$

where $\Delta t = \tilde{\lambda}/c$ is the mean free time for collisions between protons and magnetic scattering centers. Equating the acceleration rates given by equations (2.5) and (2.7), we find that

$$D = \frac{1}{4} \left(\frac{\tilde{\lambda}}{c} \right) \left(\frac{dv_\phi}{dR} \right)^2 \sim \text{s}^{-1}, \quad (2.8)$$

which establishes the nature of the diffusion coefficient governing the stochastic transport of the Fermi accelerated protons through the energy space. In the case of the relativistic particles, the heating rate due to Fermi acceleration can be obtained by averaging equation (2.5) over the particle energy and multiplying by the proton number density, which yields

$$\frac{dU}{dt} = 4 \langle \epsilon \rangle D N = 4 D U \sim \text{ergs cm}^{-3} \text{ s}^{-1}, \quad (2.9)$$

where $\langle \epsilon \rangle \equiv U/N$ is the mean proton energy.

2.3. Viscous Heating vs. Nonthermal Particle Acceleration

Although we have derived our formal results for Fermi acceleration under the assumption that the protons are relativistic, we can calculate the corresponding energy diffusion coefficient for

the thermal protons in the shear flow by replacing the relativistic particle velocity c in equation (2.8) with the typical thermal velocity $v_{\text{rms}} = \sqrt{3kT_i/m_i} = \lambda_{ii}/t_{ii}$, where λ_{ii} is the mean free path for proton-proton collisions and

$$t_{ii} = 11.4 \frac{T_i^{3/2}}{N \ln \Lambda} \sim \text{s} \quad (2.10)$$

is the associated mean free time for Coulomb logarithm $\ln \Lambda$ (see Paper I). The result obtained for the thermal diffusion coefficient is

$$D_{\text{th}} = 2.85 \frac{\tilde{\lambda}}{\lambda_{ii}} \frac{T_i^{3/2}}{N \ln \Lambda} \left(\frac{dv_\phi}{dR} \right)^2. \quad (2.11)$$

The corresponding heating rate associated with the Fermi acceleration of the thermal protons can be obtained by writing in analogy to equation (2.9)

$$\frac{dU_{\text{th}}}{dt} = 4 D_{\text{th}} U_{\text{th}} = 2.36 \times 10^{-15} \frac{\tilde{\lambda}}{\lambda_{ii}} \frac{T_i^{5/2}}{\ln \Lambda} \left(\frac{dv_\phi}{dR} \right)^2, \quad (2.12)$$

where $U_{\text{th}} = (3/2)NkT_i$ is the energy density of the thermal protons. This result for the Fermi heating rate of the thermal protons is comparable to the viscous dissipation rate computed using the usual formula $\eta_{\text{hyb}}(dv_\phi/dR)^2$ (Landau & Lifshitz 1987), where η_{hyb} is the ‘‘hybrid’’ viscosity coefficient derived in Paper I for the same physical situation considered here, but using a standard approach based upon an explicit calculation of the momentum flux in the shear flow. In the hybrid scenario, the angular momentum is carried by the protons, but the collisions occur predominantly between the protons and the magnetic field kinks. We have therefore established that the shear-driven Fermi acceleration experienced by the thermal protons is equivalent to conventional viscous heating.

The Fermi acceleration mechanism pumps energy into all of the protons residing in either the disk or the corona, since both of these regions are threaded by the shearing magnetic field. Although each region experiences the same shear, the shape of the resulting steady-state proton distribution will also depend on the degree to which the energy supplied by Fermi acceleration is thermalized via proton-proton collisions. In the disk, the proton number density is high enough for collisional thermalization to occur, resulting in a Maxwellian distribution for the disk protons (Katz 1991). Conversely, due to the low density in the corona, we do not expect thermalization to

occur very effectively there, and consequently the coronal protons are likely to have a nonthermal distribution. In § 3 we support this conclusion by carefully considering the losses occurring in the corona.

3. KINETIC EQUATION

In the general picture considered here, thermal seed protons from the accretion disk diffuse upwards into the tenuous corona, where they undergo second-order Fermi acceleration due to collisions with kinks in the local magnetic field. We assume that the field lines in the corona are anchored in the underlying disk, and that the lines (and the kinks) therefore participate in the same shearing motion as the disk itself. Under suitable conditions, the protons accelerated in the corona possess enough energy to drive a transonic electron-proton wind that can escape to infinity with a sizable asymptotic Lorentz factor. The shear-driven second-order Fermi acceleration mechanism will tend to produce a nonthermal proton energy distribution in the corona, although the shape of the distribution is also affected by particle interactions which can thermalize the relativistic protons.

3.1. Collisional Losses

The collisional losses experienced by protons in the corona occur primarily via interactions with other protons mediated by either the Coulomb force or the strong force. The ratio of the loss timescales for these two processes can be expressed as a function of the proton energy $\epsilon = \gamma m_p c^2$ using (e.g., Dermer, Miller, & Li 1996)

$$\frac{t_{\text{Coul}}}{t_{\text{pp}}} = 1225 \frac{\sigma_{\text{pp}}}{\sigma_{\text{T}}} \frac{\gamma - 1}{\beta^2 \ln \Lambda} \left(3.8 \theta_{\text{pl}}^{3/2} + \beta^3 \right), \quad (3.1)$$

where t_{Coul} is the timescale for Coulomb collisions, t_{pp} is the timescale for strong interactions, $\sigma_{\text{pp}} = 3 \times 10^{-26} \text{ cm}^2$ is the strong interaction cross section, σ_{T} is the Thomson scattering cross section, $\beta \equiv (1 - \gamma^{-2})^{1/2}$, and $\theta_{\text{pl}} \equiv kT_i/m_e c^2$, with m_e denoting the electron mass. Setting $T_i = 10^{12} \text{ K}$ and $\ln \Lambda = 25$, we find that losses due to strong interactions dominate over proton-proton Coulomb losses for all of the energetic protons, whether in the disk or the corona. This is a

direct consequence of the virial temperature of the hot disk. Conversely, in relatively cool plasmas, Coulomb losses dominate (Dermer, Miller, & Li 1996).

The energy loss rate due to strong proton-proton interactions can be written as

$$\dot{\epsilon}_{\text{loss}} = -\nu_{\text{loss}} \epsilon, \quad \nu_{\text{loss}} = \sigma_{\text{pp}} c N. \quad (3.2)$$

The direct dependence of the strong interaction loss rate upon the proton number density N implies that the collisional losses will be more severe in the dense disk midplane than in the relatively tenuous corona, and we therefore assume that the disk protons have a Maxwellian distribution with temperature T_i . The importance of collisional losses in the corona depends on the density there, and in § 6 we estimate an upper limit for the accretion rate below which the loss timescale due to strong proton-proton interactions in the corona exceeds the shear acceleration timescale. We are justified in neglecting proton losses in our calculations so long as we confine our attention to accretion rates that are well below this upper limit, which greatly exceeds the Eddington accretion rate.

In addition to the energy losses associated with proton-proton interactions, the relativistic protons in the corona also experience losses due to Coulomb coupling with the attendant electrons (which cool readily via synchrotron and inverse-Compton emission) and in principle this can limit the Lorentz factor of any resulting jet (Phinney 1982). However, so long as the electron and proton number densities are equal, proton-electron Coulomb losses are less important than proton-proton Coulomb losses (Schmidt 1966), which are negligible compared with the losses due to strong proton-proton interactions according to equation (3.1). This conclusion must be modified if copious electron-positron pair production takes place in the corona, since this process can significantly enhance the proton-electron cooling rate by increasing the number of electrons (and positrons) per proton. We address this issue in § 6 by demonstrating that the optical thickness of the corona to photon-photon pair production is much less than unity, implying that pair production can be safely ignored. In principle, the protons also lose energy via *direct* synchrotron and inverse-Compton emission, but these processes are unimportant in the proton energy range of interest here.

3.2. Particle Distribution in the Corona

The transport equation governing the energy distribution of the relativistic protons in the corona can be obtained by incorporating a source term and an escape term into equation (2.2) and substituting for the energy diffusion coefficient \mathcal{D} using equation (2.6), which yields

$$\frac{\partial f}{\partial t} = \frac{D_1}{c^2} \frac{\partial}{\partial \epsilon} \left(\epsilon^4 \frac{\partial f}{\partial \epsilon} \right) - \frac{f}{t_1} + \frac{\dot{N}_1 \delta(\epsilon - \epsilon_i)}{\epsilon_i^2}, \quad (3.3)$$

where the subscript “1” will be used to denote parameters associated with the corona, and t_1 represents the mean time protons spend in the corona before escaping into the wind. The final term in equation (3.3) describes the injection of monoenergetic protons with energy ϵ_i at a rate per unit volume equal to \dot{N}_1 . Physically, the “injection” process corresponds to the diffusion of seed protons from the underlying disk up into the corona. Note that a Maxwellian cannot be recovered from equation (3.3) because it does not contain a collisional loss term; our neglect of collisional losses is reasonable for sufficiently low accretion rates, as discussed in § 6. We can relate the escape timescale t_1 to the coherence length in the corona $\tilde{\lambda}_1$ using

$$t_1 \equiv \frac{h}{v_1} = \frac{h^2}{c \tilde{\lambda}_1}, \quad (3.4)$$

where h is the vertical thickness of the corona and the diffusion velocity for protons escaping from the corona into the wind is given by

$$v_1 \equiv \frac{c \tilde{\lambda}_1}{h} \sim \frac{\kappa_1}{h}, \quad (3.5)$$

with

$$\kappa_1 \equiv \frac{1}{3} c \tilde{\lambda}_1 \quad (3.6)$$

denoting the associated spatial diffusion coefficient (e.g., Reif 1965). We shall assume throughout that the corona has no vertical structure.

Before solving equation (3.3) for the proton energy distribution in the corona, it is interesting to calculate the mean energy of the protons in the corona based on fundamental properties of the Fermi acceleration process. As a first step, consider the time evolution of the mean energy of a

single proton injected into the corona with energy ϵ_i at time $t = 0$. By integrating equation (2.5) we find that the mean energy of this proton (while it remains in the corona) varies as

$$\bar{\epsilon}(t) = \epsilon_i e^{4D_1 t}. \quad (3.7)$$

In the absence of losses, the mean energy of the proton therefore increases without bound until the proton escapes from the corona by diffusing out into the wind. Next we make use of the observation that the mean energy of the protons in the corona is equal to the mean energy of the protons escaping from the corona, which is a consequence of the fact that the escape timescale t_1 is independent of the proton energy. We can therefore compute the mean energy of the protons in the corona by calculating the average energy of the single proton at the time that it escapes from the corona. This yields

$$\langle \epsilon \rangle = \int_0^\infty \bar{\epsilon}(t) e^{-t/t_1} \frac{dt}{t_1}, \quad (3.8)$$

where the last factor expresses the probability that the proton will remain in the corona until time t and then escape during the subsequent time interval dt . Substituting for $\bar{\epsilon}(t)$ in equation (3.8) using equation (3.7) and integrating yields

$$\langle \epsilon \rangle = \frac{\epsilon_i}{1 - y}, \quad (3.9)$$

where we have defined the y -parameter for the Fermi process as

$$y \equiv 4 D_1 t_1 = \frac{\langle \dot{\epsilon}_{\text{shear}} \rangle}{\epsilon} t_1, \quad (3.10)$$

and made use of equation (2.5) to arrive at the final result.

In the analogous case of photon Comptonization, the y -parameter measures the mean fractional energy gain experienced by soft photons scattering in a medium of hot electrons, and y must exceed unity for significant distortion of the input spectrum to occur (e.g., Rybicki & Lightman 1979). However, for the shear-driven Fermi acceleration process treated here, the mean proton energy $\langle \epsilon \rangle$ *diverges* as $y \rightarrow 1$. From a physical point of view, the divergence of $\langle \epsilon \rangle$ is due to the fact that an infinitesimal number of protons remain in the corona long enough to gain an infinite amount of energy, which leads to a logarithmic divergence in the total energy density as

$y \rightarrow 1$. Hence in our model y cannot exceed (or even equal) unity. The apparent contradiction is due to the fact that electron recoil losses are included in the Comptonization model, whereas the corresponding loss mechanisms for the protons (direct synchrotron and inverse-Compton emission) are unimportant in the context of the particle transport model considered here. Note that the Fermi y -parameter is independent of the mean free path $\tilde{\lambda}_1$, since it can be rewritten as

$$y = \left(\frac{h}{c} \frac{dv_\phi}{dR} \right)^2, \quad (3.11)$$

where we have used equations (2.8) and (3.4). The detailed numerical results presented in § 7 indicate that $y \sim 1$ throughout most of the corona, and therefore we conclude based on equation (3.9) that the average energy of the protons in the corona is much higher than that in the disk.

In a steady-state ($\partial/\partial t \rightarrow 0$), the transport equation (3.3) can be written in the form

$$D_1 \epsilon^2 \frac{\partial^2 f}{\partial \epsilon^2} + 4 D_1 \epsilon \frac{\partial f}{\partial \epsilon} - \frac{f}{t_1} = - \frac{\dot{N}_1 \delta(\epsilon - \epsilon_i)}{\epsilon_i^2}. \quad (3.12)$$

The homogeneous equation obtained when $\epsilon \neq \epsilon_i$ admits the power-law solutions

$$G_A(\epsilon, \epsilon_i) \equiv \frac{\dot{N}_1}{\epsilon_i^3} \frac{(\epsilon/\epsilon_i)^{m_A}}{D_1 (m_A - m_B)}, \quad G_B(\epsilon, \epsilon_i) \equiv \frac{\dot{N}_1}{\epsilon_i^3} \frac{(\epsilon/\epsilon_i)^{m_B}}{D_1 (m_A - m_B)}, \quad (3.13)$$

where

$$m_A \equiv -\frac{3}{2} + \sqrt{\frac{9}{4} + \frac{4}{y}}, \quad m_B \equiv -\frac{3}{2} - \sqrt{\frac{9}{4} + \frac{4}{y}}. \quad (3.14)$$

Under the restriction $y < 1$ required in order to obtain a finite value for $\langle \epsilon \rangle$ using equation (3.9), we find that $m_A > 1$ and $m_B < -4$. Second-order Fermi acceleration is a stochastic process, and therefore some of the protons lose energy and some gain energy. It follows from the constraints on m_A and m_B that G_A describes the distribution for $\epsilon \leq \epsilon_i$ and G_B describes the distribution for $\epsilon \geq \epsilon_i$. The result obtained for the Green's function is therefore

$$G(\epsilon, \epsilon_i) = \begin{cases} G_A(\epsilon, \epsilon_i), & \epsilon \leq \epsilon_i, \\ G_B(\epsilon, \epsilon_i), & \epsilon \geq \epsilon_i. \end{cases} \quad (3.15)$$

The total particle number density associated with the Green's function is given by

$$N_G \equiv \int_0^\infty \epsilon^2 G(\epsilon, \epsilon_i) d\epsilon = \dot{N}_1 t_1, \quad (3.16)$$

in agreement with the result obtained by operating on equation (3.12) with $\int_0^\infty \epsilon^2 d\epsilon$. We can also integrate the Green's function to obtain the associated energy density,

$$U_G \equiv \int_0^\infty \epsilon^3 G(\epsilon, \epsilon_i) d\epsilon = \frac{\dot{N}_1 \epsilon_i t_1}{1 - 4 D_1 t_1}, \quad (3.17)$$

which can be verified by operating on equation (3.12) with $\int_0^\infty \epsilon^3 d\epsilon$. We remind the reader of the arguments made immediately following equation (2.4), concerning the lower bound of integration in equations (3.16) and (3.17). The mean energy of the protons is therefore

$$\langle \epsilon \rangle = \frac{U_G}{N_G} = \frac{\epsilon_i}{1 - 4 D_1 t_1}, \quad (3.18)$$

in agreement with equation (3.9).

The Green's function given by equation (3.15) represents the response of equation (3.12) to the diffusion of monoenergetic seed particles from the disk into the corona. The particles injected into the corona via the diffusion process appear at a rate per unit volume equal to \dot{N}_1 . Although we have assumed that the seed particles are monoenergetic, in reality the protons diffusing into the corona have a thermal distribution of energies corresponding to the disk temperature T_i . However, this does not cause any difficulties because equation (3.12) is linear, and therefore the proton distribution resulting from the diffusion of the thermal disk protons into the corona can be obtained by convolving the Green's function with the Maxwellian source distribution. We can accomplish this formally by writing

$$f(\epsilon) = \int_0^\infty \frac{G(\epsilon, \epsilon_i)}{\dot{N}_1} S(\epsilon_i, T_i) d\epsilon_i, \quad (3.19)$$

where $S(\epsilon_i, T_i) d\epsilon_i$ gives the number of protons in the energy range between ϵ_i and $\epsilon_i + d\epsilon_i$ appearing in the corona per unit volume per unit time due to the Maxwellian source. In this paper it is our intention to focus mainly on the dynamics of the disk/corona/wind system, and we therefore defer a detailed calculation of the coronal proton distribution to a subsequent paper. However, we expect that the energy distribution of the protons in the corona will be described by the power law behavior $f \propto \epsilon^{m_B}$ at high energies, with the power-law index m_B given by equation (3.14). At lower energies (approaching the mean energy of the disk protons), the coronal proton distribution will retain a Maxwellian form.

4. DISK-CORONA STRUCTURE

In order to obtain a coupled disk/corona/wind model, we must understand how the disk structure influences the diffusion of the thermal seed protons into the corona. In the scenario envisioned here, the protons diffusing into the corona have a Maxwellian energy distribution at the local disk temperature $T_i(R)$, where R is the cylindrical radius at the point of interest in the corona. The mean energy of the escaping protons is equal to $(3/2)kT_i$, assuming that the disk protons are nonrelativistic. Since the mean energy of the escaping protons is equal to the mean energy of the protons remaining in the disk, the escape of protons from the disk has no effect on the disk temperature. However, this process will affect the pressure and density distributions in the disk, and the loss of mass will cause the accretion rate to decrease with decreasing radius. We must therefore perform a self-consistent calculation of the structures of the disk and the corona.

4.1. Disk Structure

Motivated by earlier studies of two-temperature flows (e.g., Shapiro, Lightman, & Eardley 1976; Eilek & Kafatos 1983; Paper 1), we adopt the α -disk model (see Frank, King, & Raine 1992 for a review). In particular, we assume that the ions are virially hot ($T_i \sim 10^{12}$ K), while the electrons are able to cool effectively via inverse-Compton and synchrotron emission and therefore have a much lower temperature ($T_e \sim 10^9$ K). For simplicity, we shall assume that the disk possesses no vertical structure, and that it is composed of fully-ionized hydrogen, with internal energy density U_0 , pressure $P_0 = (\gamma_0 - 1)U_0$, proton number density N_0 , and mass density $\rho_0 = m_p N_0$. The quantities U_0 , P_0 , N_0 , ρ_0 , and the disk half-thickness H are all functions of the cylindrical radius R . The nonrelativistic value of the adiabatic index ($\gamma_0 = 5/3$) will be used throughout to describe the thermodynamic properties of the gas in the disk. The geometry of the disk-corona system is indicated in Figure 2. According to the virial theorem, the internal energy of the disk protons is equal to half their gravitational potential energy, so that

$$U_0 = \frac{1}{2} \frac{N_0 m_p c^2}{R_* - 2}, \quad (4.1)$$

where $R_* \equiv R c^2/GM$ is the dimensionless radius. In writing equation (4.1), we have approximated

the effects of general relativity by using the pseudo-Newtonian prescription for the gravitational potential (Paczynski & Wiita 1980).

The Keplerian azimuthal velocity corresponding to the pseudo-Newtonian potential is given by (Paczynski & Wiita 1980)

$$\frac{v_\phi}{c} = \frac{\sqrt{R_*}}{R_* - 2}, \quad (4.2)$$

and we can use equation (4.1) to write the classical adiabatic sound speed in the disk as

$$s_0 \equiv \sqrt{\frac{\gamma_0 P_0}{\rho_0}} = c \sqrt{\frac{\gamma_0(\gamma_0 - 1)}{2(R_* - 2)}}. \quad (4.3)$$

By combining equations (4.2) and (4.3) we can express the azimuthal Mach number as

$$\mathcal{M}_\phi \equiv \frac{v_\phi}{s_0} = \sqrt{\frac{2}{\gamma_0(\gamma_0 - 1)} \frac{R_*}{R_* - 2}}. \quad (4.4)$$

The usual scaling relations for the disk half-thickness H and the radial drift velocity v_R remain valid for a flow governed by the pseudo-Newtonian potential, so that we have (see Frank, King, & Raine 1992)

$$H \sim \mathcal{M}_\phi^{-1} R, \quad (4.5)$$

$$v_R \sim \alpha \mathcal{M}_\phi^{-1} s_0. \quad (4.6)$$

Combining these relations with equations (4.3) and (4.4), we find that the radial velocity and the height are given by

$$\frac{v_R}{c} = \alpha \frac{\gamma_0(\gamma_0 - 1)}{2\sqrt{R_*}}, \quad (4.7)$$

$$\frac{H}{R} = \sqrt{\frac{\gamma_0(\gamma_0 - 1)}{2} \frac{R_* - 2}{R_*}}. \quad (4.8)$$

Note that $H/R \ll 1$ throughout the flow, and that v_R is defined to be positive for infall.

4.2. Disk-Corona Connection

Second-order Fermi acceleration of the relativistic protons takes place in the corona as a result of multiple collisions with magnetic scattering centers (kinks) dragged along by field lines anchored in the shearing disk. The corona has thickness h , energy density U_1 , pressure $P_1 = (\gamma_1 - 1)U_1$, proton number density N_1 , and mass density ρ_1 , where $\gamma_1 = 4/3$ since the protons are

relativistic. In keeping with our approximate model for the disk (which has no vertical structure), we assume for simplicity that the corona also has no vertical structure. Standard disk/corona models require vertical hydrostatic equilibrium, and this leads to the conclusion that the gas pressure in the disk exceeds that in the corona. However, in the model considered here, the gas in the corona has positive specific energy as a consequence of Fermi acceleration, and therefore the protons in the corona are not bound to the black hole. Hence we cannot use hydrostatic equilibrium to determine the pressure in the corona. As an alternative prescription, we invoke a pressure balance between the disk and the corona ($P_0 = P_1$) so that no net force exists between these regions. This assumption is physically reasonable since any imbalance would be quickly removed by sound waves propagating across the disk/corona interface.

It follows from the statement of pressure equilibrium and the values of γ_0 and γ_1 that

$$U_1 = 2U_0. \quad (4.9)$$

In the absence of a pressure gradient, the transport of seed particles from the disk to the corona occurs primarily via spatial diffusion, and the efficiency of the diffusion process depends on the degree to which the field is tangled in the disk. Likewise, the escape of relativistic protons from the corona into the base of the wind can also be treated as a diffusive process, with an efficiency that depends on the degree to which the field is tangled in the corona. The efficiency of diffusion is determined primarily by the coherence length of the magnetic field, $\tilde{\lambda}$. In most simulations of fully-developed MHD turbulence driven by the magnetic shearing instability, $\tilde{\lambda}$ scales as a fixed fraction of the size of the computational “box,” which corresponds to H in the disk or to h in the corona (Brandenburg et al. 1995; Hawley, Gammie, & Balbus 1995; Matsumoto & Tajima 1995). In their linear stability analysis, Matsumoto & Tajima (1995) find that the fastest growing modes have a $\tilde{\lambda} \sim 0.1 L$, where L is the characteristic size of the computational box. We therefore model the magnetic field by introducing the two parameters

$$\xi_0 \equiv \frac{\tilde{\lambda}_0}{H}, \quad \xi_1 \equiv \frac{\tilde{\lambda}_1}{h}, \quad (4.10)$$

which describe the degree of tangling in the disk and the corona, respectively. Note that for a diffusive prescription to apply, clearly ξ_0 and ξ_1 cannot exceed unity.

We can use equations (3.5) and (4.10) to define the diffusion velocities in the disk and the corona, respectively, as

$$v_0 \equiv \xi_0 c, \quad v_1 \equiv \xi_1 c. \quad (4.11)$$

Vertical hydrostatic equilibrium in the disk is maintained so long as $v_0 \ll v_R$, which is seen to be satisfied in our results. Conservation of the proton flux in a column connecting the disk to the corona implies that the proton number densities in the disk (N_0) and in the corona (N_1) are related via the one-dimensional continuity equation

$$N_1 v_1 = N_0 v_0. \quad (4.12)$$

It follows from equations (4.11) and (4.12) that the densities in the two regions are related by

$$\frac{N_1}{N_0} = \frac{\xi_0}{\xi_1}. \quad (4.13)$$

We generally expect to find that $N_1/N_0 < 1$ since the particles populating the corona escape from the disk via diffusion. In this case our assumption of pressure equilibrium ($P_0 = P_1$) implies that the energy per particle in the corona exceeds that in the disk, which is crucial for the formation of a relativistic wind (e.g., Contopoulos & Kazanas 1995) as discussed in § 5.

The acceleration of the protons in the corona obviously requires a substantial source of energy, and in our model we implicitly assume that the energy is supplied to the corona via the Poynting flux of the shearing magnetic field, which drains kinetic energy from the Keplerian accretion disk via viscous dissipation. Although it is not our goal here to develop a detailed model for the magnetic field in the disk and the corona, we can use our assumption of disk/corona pressure equilibrium along with our results concerning Fermi acceleration to constrain the thickness of the corona, h , based upon energy considerations. Let us assume for the moment that the protons diffusing into the corona are monoenergetic, so that we can use equations (3.16) and (3.17) to write

$$N_1 = N_G = \dot{N}_1 t_1, \quad U_1 = U_G = \frac{\dot{N}_1 \epsilon_i t_1}{1 - 4 D_1 t_1}, \quad (4.14)$$

where \dot{N}_1 denotes the rate per unit volume at which particles with energy ϵ_i diffuse into the corona and the escape timescale for the protons in the corona is given by

$$t_1 \equiv \frac{h}{v_1} = \frac{h}{c \xi_1}. \quad (4.15)$$

Combining equations (4.13) and (4.14) with the pressure equilibrium condition expressed by equation (4.9) yields

$$2 = \frac{U_1}{U_0} = \frac{\xi_0}{\xi_1} \frac{1}{1-y}, \quad (4.16)$$

where $y = 4 D_1 t_1$ according to equation (3.10) and we have used the fact that $U_0 = N_0 \epsilon_i$. Although we have assumed monoenergetic injection in deriving equation (4.16), the result is valid for protons injected with an arbitrary energy spectrum. We can use equation (2.8) to obtain another expression for D_1 under the assumption of Keplerian flow. Incorporating the pseudo-Newtonian potential (eq. [4.2]) and assuming that the velocity differential between the footpoints of the tangled magnetic field is transmitted unchanged from the disk to the corona, we obtain

$$D_1 = \frac{\tilde{\lambda}_1 c}{R_g^2} \frac{(R_* + 2)^2}{16 R_* (R_* - 2)^4}, \quad (4.17)$$

where $R_g \equiv GM/c^2$. Eliminating D_1 between equations (4.16) and (4.17) and setting $\tilde{\lambda}_1 = h\xi_1$ and $t_1 = h/(\xi_1 c)$, we find that the extent of the acceleration region h is given by

$$\frac{h}{R_g} = 2 \sqrt{R_*} \frac{(R_* - 2)^2}{R_* + 2} \left(1 - \frac{\xi_0}{2\xi_1}\right)^{1/2}. \quad (4.18)$$

4.3. Variation of the Accretion Rate

The escape of protons from the accretion flow into the wind via the corona will cause the disk accretion rate \dot{M} to decrease with decreasing radius. Since the structure of the disk (and therefore the conditions in the corona) will in turn be influenced by the variation of the accretion rate, we must determine \dot{M} in a self-consistent manner. The continuity equation relating a differential change in the disk accretion rate to a differential change in the wind mass loss rate is given by

$$d\dot{m} = -\frac{1}{2} d\dot{M}, \quad (4.19)$$

where \dot{m} denotes the mass loss rate into one of the two winds emanating from the disk-corona system. The factor of 1/2 appears because we have only taken into account the mass lost into one of the winds. The flux of protons leaving the disk is equal to $N_0 v_0$, which must equal $N_1 v_1$ by virtue of equation (4.12). It follows that the continuity equation for the disk can be written as

$$d\dot{M} = 2 \cdot m_p N_1 v_1 \cdot 2\pi R dR. \quad (4.20)$$

The accretion rate can also be expressed in terms of the disk parameters as

$$\dot{M} = 2\pi R \cdot 2H \cdot m_p N_0 v_R, \quad (4.21)$$

which can be combined with equations (4.7), (4.8), and (4.20) to obtain a differential equation for the variation of the accretion rate,

$$\frac{d \ln \dot{M}}{dR} = \left(\frac{9}{5}\right)^{3/2} \frac{\xi_0}{\alpha} \frac{1}{\sqrt{R_* - 2}} \frac{1}{R_g}, \quad (4.22)$$

with solution

$$\frac{\dot{M}(R)}{\dot{M}_{\text{out}}} = \exp \left\{ 2 \left(\frac{9}{5}\right)^{3/2} \frac{\xi_0}{\alpha} \left[\left(\frac{R}{R_g} - 2\right)^{1/2} - \left(\frac{R_{\text{out}}}{R_g} - 2\right)^{1/2} \right] \right\}, \quad (4.23)$$

where R_{out} is the largest radius at which shear acceleration in the corona is strong enough to expel particles into the wind (i.e., the wind “turn-on” radius), and $\dot{M}_{\text{out}} \equiv \dot{M}(R_{\text{out}})$. With $\dot{M}(R)$ determined, we can calculate $\dot{m}(R)$ using equation (4.19), which yields

$$\dot{m}(R) = \frac{\dot{M}_{\text{out}} - \dot{M}(R)}{2}. \quad (4.24)$$

Since no mass is lost into the wind at radii beyond R_{out} , we can interpret \dot{M}_{out} as the accretion rate supplied to the disk at a large distance from the central object. Equation (4.23) expresses the subsequent decrease in the disk accretion rate \dot{M} as a result of the expulsion of mass from radius R_{out} inwards. Note that in deriving this result we have assumed that ξ_0 is independent of radius and we have set $\gamma_0 = 5/3$. We consider the procedure for calculating the wind turn-on radius R_{out} in § 6 where specific applications are made.

5. RELATIVISTIC WIND FORMATION

Protons energized via second-order Fermi acceleration in the shearing corona will escape via spatial diffusion, which tends to oppose the density gradient and will therefore transport particles preferentially in the “upward” direction, leading to the formation of a rotating, transonic wind. In the picture developed here, the diffusion velocity v_1 for the protons escaping from the corona is set equal to the vertical component of the flow velocity at the base of the wind, so that the corona and

the wind merge smoothly. The assumption of a smooth wind-corona merger is physically reasonable since there is no “hard” interface between the two regions. The outflowing proton distribution is expected to remain isotropic in the comoving frame due to interactions with magnetic kinks, lending validity to a fluid description of the wind plasma. As the gas moves away from the central object, it expands and cools adiabatically, since protons are not subject to strong radiative losses. Through the expansion process, the internal energy of the protons is gradually converted into kinetic energy of the outflow. In order for the gas to escape to infinity, the internal energy per unit mass in the corona must be super-virial, so that the corona is not bound to the black hole. This is equivalent to the statement that the *total* energy per unit mass in the corona must be positive (Blandford & Begelman 1999).

The detailed streamline shape which the outflow follows depends on the nature of the collimation mechanism, which is far from clear. Collimation of the flow could occur via magnetic hoop stresses if the jet is enveloped by toroidal magnetic fields in a magnetic “cocoon” (Blandford & Payne 1982; Contopoulos & Lovelace 1994; Ustyugova et al. 1995). The cocoon models rely upon magneto-centrifugal acceleration and assume the existence of a large-scale magnetic field that guides the jet. The non-magnetic models of Daly & Marscher (1988) display an oscillating cross section which depends upon the details of the balance between the gas pressure in the jet and the pressure of the external medium. Given the large uncertainty in the details of the outflow cross section, we present a theory in which the streamline shape is left arbitrary. As in Chakrabarti (1985), the inherently three-dimensional problem is reduced to a two-dimensional problem by assuming azimuthal symmetry. The two-dimensional problem, in turn, is reduced to a one-dimensional problem by prescribing the shape of the “streamtube,” which is the locus of streamlines that the gas parcels follow from a given starting radius in the corona. Although the magnetic field may play an important role in determining the streamtube shape, we assume here that the magnetic pressure is negligible compared with the pressure of the protons. The streamtube shape is left arbitrary in our theory, although in our specific examples we present results associated with conical outflow (e.g., Mannheim 1993; Blandford & Konigl 1979), with a variety of opening angles.

5.1. Wind Structure Equations

While viscous dissipation plays a crucial role in determining the structure of the underlying accretion disk, we do not expect shear stresses to be important in the wind because the density of the gas drops very rapidly during the expansion. We therefore assume that the rotating wind emanating from the corona is inviscid, so that the specific angular momentum λ is conserved along the streamtubes. We further assume that the base of the wind (the corona) corotates with the Keplerian disk, and that this corotation is enforced by the magnetic field lines that thread the corona and are anchored in the disk. We therefore set λ equal to its Keplerian value at the base of a streamtube as part of our condition for smoothly merging the corona with the wind, and consequently λ will depend on the starting radius in the corona.

The streamtube shape is defined by postulating the cylindrical radius of the streamline r to be a specified function f of the height above the disk midplane z and the cylindrical starting radius at the base of the flow R ,

$$r \equiv f(R, z). \quad (5.1)$$

Defining z_1 to be the height at which the corona connects with the wind, it follows that

$$R = f(R, z_1). \quad (5.2)$$

The components of the flow velocity in the wind in the \hat{z} , \hat{r} , and $\hat{\phi}$ directions will be denoted by v , u , and w , respectively.

Introducing the convenient definitions

$$f_z \equiv \left(\frac{\partial f}{\partial z} \right)_R, \quad f_R \equiv \left(\frac{\partial f}{\partial R} \right)_z, \quad f_{zR} \equiv \frac{\partial^2 f}{\partial z \partial R}, \quad f_{zz} \equiv \frac{\partial^2 f}{\partial z^2}, \quad (5.3)$$

we note that

$$u = v f_z, \quad (5.4)$$

and therefore the bulk Lorentz factor of the flow is given by

$$\Gamma = \frac{c}{\sqrt{c^2 - w^2 - (1 + f_z^2)v^2}}. \quad (5.5)$$

Utilizing the relativistically correct definition of the angular momentum per unit mass,

$$\lambda = \Gamma r w, \quad (5.6)$$

and assuming that the wind is inviscid ($\lambda = \text{constant}$), we can rewrite our expression for Γ as

$$\Gamma^2 = \frac{c^2 + \lambda^2/f^2}{c^2 - v^2(1 + f_z^2)}. \quad (5.7)$$

In our calculations, we set the specific angular momentum equal to its Keplerian value in the pseudo-Newtonian potential (Paczynski & Wiita 1980),

$$\lambda = \frac{GM}{c} \frac{R_*^{3/2}}{R_* - 2}. \quad (5.8)$$

If we restrict our attention to cylindrical annuli along the flow, then the conservation equation for the proton number density in the wind (N) can be written as (e.g., Mihalas & Mihalas 1984)

$$\Gamma r N v dr = \text{constant}. \quad (5.9)$$

This expression, which describes the conservation of z -directed particle flux, can be rewritten using equations (5.1) and (5.3) as

$$N v = N_1 v_1 \frac{\Gamma_1}{\Gamma} \frac{R}{f} \frac{1}{f_R}, \quad (5.10)$$

where, as before, the subscript “1” denotes quantities measured in the corona, which is also the base of the wind. In the case of purely radial outflow, with $f(R, z) = Rz/z_1$, it can be verified that the number conservation equation reduces to the standard mass conservation equation for relativistic Bondi flow (Subramanian 1997).

Since the outflow is powered by the pressure of the relativistic protons, we set the adiabatic index in the wind equal to the relativistic value used in the corona, $\gamma_1 = 4/3$. As the gas expands, the protons cool adiabatically because losses due to Coulomb coupling with the electrons or the direct emission of radiation are negligible. The classical adiabatic sound speed s in the wind can therefore be expressed as a function of z and v using

$$s \equiv \left(\frac{\gamma_1 P}{N m_p} \right)^{1/2} = s_1 \left(\frac{\Gamma_1}{\Gamma} \frac{v_1}{v} \frac{R}{f} \frac{1}{f_R} \right)^{(\gamma_1 - 1)/2}, \quad (5.11)$$

where the final result follows from equation (5.10) in combination with the adiabatic law $P \propto N^{\gamma_1 - 1}$. We remind the reader that the classical adiabatic sound speed s is related to the relativistic sound speed a by (Weinberg 1972)

$$a^2 = \frac{(\gamma_1 - 1) c^2 s^2}{(\gamma_1 - 1) c^2 + s^2}. \quad (5.12)$$

When the flow is adiabatic as assumed here, the wind obeys the relativistic Bernoulli equation (Mihalas & Mihalas 1984; Contopoulos & Kazanas 1995)

$$\left(1 + \frac{s^2}{c^2} \frac{1}{\gamma_1 - 1}\right) \Gamma - \frac{R_g}{\sqrt{f^2 + z^2} - 2R_g} \equiv B(v, z) = \text{constant}, \quad (5.13)$$

where the second term on the left-hand side represents the pseudo-Newtonian potential and the quantity $\sqrt{f^2 + z^2}$ denotes the spherical radius. In adiabatic outflows, the Bernoulli function $B(v, z)$ is conserved along streamtubes, although it varies as a function of the starting radius in the corona. The Bernoulli constant is equal to the dimensionless energy per unit mass at the base of the wind, and it must therefore be positive if the flow is to escape to infinity (Blandford & Begelman 1999). Once the streamtube function f has been specified, the Lorentz factor Γ appearing in equation (5.13) can be expressed as a function of z and v using equation (5.7) and therefore equation (5.13) can be used to determine the variation of the vertical velocity v as a function of the height z . Note that in order to solve for the velocity we must first determine the value of the Bernoulli constant corresponding to critical flow.

5.2. Critical Point Conditions

In order for the outflow to reach an infinite distance from the central mass, the velocity must increase monotonically as a function of radius. This requires the wind to pass through a sonic point, which is a critical point of the governing differential equation as was first noted by Bondi (1952) in his analysis of spherically symmetric, nonrelativistic flows. We can derive the appropriate set of critical point conditions by differentiating $B(v, z)$ with respect to z and v , which yields an equation of the form

$$\frac{dv}{dz} = \frac{\partial B / \partial z}{\partial B / \partial v}. \quad (5.14)$$

Critical points occur where the numerator and the denominator of equation (5.15) vanish simultaneously. Setting $\partial B/\partial v = 0$ yields

$$v_c^2 [1 + f_z^2(R, z_c)] = a_c^2 = \frac{c^2 (\gamma_1 - 1) s_c^2}{(\gamma_1 - 1) c^2 + s_c^2}, \quad (5.15)$$

where the subscript “c” denotes quantities measured at the critical point, $z = z_c$. This equation implies that the velocity in the (r, z) plane is equal to the relativistic sound speed at $z = z_c$, which is analogous to the condition $v_c = s_c$ encountered in nonrelativistic, nonrotating flows. Setting $\partial B/\partial z = 0$ at the critical point yields the additional constraint

$$\begin{aligned} & \left(1 + \frac{2 - \gamma_1}{\gamma_1 - 1} \frac{s^2}{c^2}\right) \frac{\Gamma f_z f^2}{f^2 + \lambda^2/c^2} \left(\Gamma^2 v^2 f_{zz} - \frac{\lambda^2}{f^3}\right) - \Gamma s^2 \left(\frac{f_z}{f} + \frac{f_{zR}}{f_R}\right) \\ & + \frac{(f f_z + z) R_g c^2}{\sqrt{f^2 + z^2} (\sqrt{f^2 + z^2} - 2 R_g)^2} \Big|_{z=z_c} = 0. \end{aligned} \quad (5.16)$$

Since the Bernoulli function is conserved along streamtubes, we can obtain another useful relation by writing

$$B(v_1, z_1) = B(v_c, z_c), \quad (5.17)$$

which is a statement of energy conservation. The sound speed at the base of the flow, s_1 , can be expressed in terms of quantities measured at the critical point using equation (5.11), which yields

$$s_1 = s \left(\frac{\Gamma}{\Gamma_1} \frac{v}{v_1} \frac{f}{R} f_R \right)^{(\gamma_1 - 1)/2} \Big|_{z=z_c}. \quad (5.18)$$

At this juncture, given a streamtube function $f(R, z)$ and values for the starting radius R , the starting height z_1 , and the starting velocity v_1 at the base of the wind, equations (5.15), (5.16), (5.17), and (5.18) can be solved simultaneously for z_c , v_c , s_c , and s_1 . Hence s_1 is determined by the critical conditions once v_1 and z_1 are specified.

5.3. Corona Structure Conditions

In addition to the critical conditions developed in § 5.2, we can obtain another constraint based on the requirement that the wind joins smoothly onto the corona at $z = z_1$, which expresses the fact that there is no real boundary between these regions. In particular, we need to ensure that the classical sound speed s_1 calculated using equation (5.18) is equal to the same quantity

computed using the virial model that describes the coupled disk/corona system, from which we can derive

$$s_1^2 = \frac{\gamma_1 P_1}{N_1 m_p} = \frac{v_1}{v_0} \frac{\gamma_1 (\gamma_1 - 1) c^2}{R_* - 2}, \quad (5.19)$$

where we have used equations (4.1), (4.9), and (4.12) to achieve the final result. Using equations (4.8), (4.11), and (4.18), we can also obtain an equation for the starting height in the corona (z_1) based on the geometrical constraint $z_1 = h + H$, which yields

$$\frac{z_1}{R_g} = \sqrt{R_*} \left[\frac{2(R_* - 2)^2}{R_* + 2} \sqrt{1 - \frac{v_0}{2v_1}} + \sqrt{\frac{\gamma_0(\gamma_0 - 1)(R_* - 2)}{2}} \right]. \quad (5.20)$$

Treating $\xi_0 \equiv v_0/c$ as a free parameter, equations (5.15), (5.16), (5.17), (5.18), (5.19), and (5.20) constitute an implicit set of simultaneous equations for the variables $(v_1, z_1, s_1, v_c, z_c, s_c)$ describing the critical structure of the wind originating at cylindrical radius R in the corona. Once the critical structure is established, the vertical velocity v can be calculated as a function of the height z by solving equation (5.13) with the Bernoulli constant set equal to $B(v_1, z_1)$. The disk model presupposes a value for α , and in the applications considered here we will set $\alpha = 1$ in order to simulate the effects of rapid infall close to the black hole.

5.4. Asymptotic Lorentz Factor

As the energetic proton distribution emerges from the vicinity of the central object, it cools adiabatically and expends its internal energy by accelerating the fluid. At very large distances, the internal energy of the protons becomes negligible due to the expansion and therefore the sound speed s vanishes. Since the gravitational potential of the central mass also vanishes at large distances, it follows from equation (5.13) that once we have a critical solution, the asymptotic Lorentz factor $\Gamma_\infty(R)$ for particles entering the wind at cylindrical radius R is equal to the Bernoulli constant,

$$\Gamma_\infty(R) = B(v_1, z_1) = \Gamma_1 \left(1 + \frac{s_1^2}{c^2} \frac{1}{\gamma_1 - 1} \right) - \frac{R_g}{\sqrt{R^2 + z_1^2} - 2R_g}. \quad (5.21)$$

Far from the central mass, the outflow can be regarded as a cold proton beam moving with bulk Lorentz factor $\Gamma_\infty(R)$. Hence the asymptotic Lorentz factor is a simple indicator of the energy per unit mass possessed by jet particles originating at radius R .

6. MODEL SELF-CONSISTENCY CONDITIONS

We have seen that in order to escape from the vicinity of the black hole, the wind must satisfy critical conditions that depend on the streamtube shape, and ultimately on the nature of the collimation mechanism. When these conditions are met, particles reach an infinite distance with an asymptotic Lorentz factor Γ_∞ that can greatly exceed unity, in which case the “wind” has essentially transformed into a relativistic jet. In addition to the critical conditions, the model must also satisfy a set of self-consistency conditions associated with (i) radial advection in the corona; (ii) collisional losses in the corona; (iii) photon-photon pair production in the corona; and (iv) limits on the total kinetic power carried by the jet.

6.1. Acceleration vs. Advection

The protons in the corona are accelerated via collisions with kinks in the tangled magnetic field. Since the footpoints of the tangled field lines are embedded in the disk, they are dragged into the black hole with the radial velocity v_R given by equation (4.7). This radial motion is in addition to the shearing motion associated with the variation of the azimuthal velocity v_ϕ given by equation (4.2). We must presume that the radial motion of the field lines is transmitted to the particles in the corona along with the shear motion. For acceleration to take place in the corona, we therefore argue that the infall timescale for radial advection must exceed the acceleration timescale for the second-order Fermi (shear acceleration) process. The characteristic timescale for the shear acceleration process can be computed by applying equation (2.5) in the corona, yielding

$$t_{\text{shear}} \equiv \frac{\epsilon}{\dot{\epsilon}_{\text{shear}}} = \frac{1}{4 D_1}, \quad (6.1)$$

or, utilizing equations (4.11), (4.17), and (4.18),

$$t_{\text{shear}} = \frac{2 R_g R_*^{1/2} (R_* - 2)^2}{(R_* + 2) v_1} \left(1 - \frac{v_0}{2 v_1}\right)^{-1/2}. \quad (6.2)$$

The infall timescale is given by

$$t_{\text{infall}} \equiv \frac{R}{v_R} = \frac{2 R_g R_*^{3/2}}{\alpha \gamma_0 (\gamma_0 - 1) c}, \quad (6.3)$$

where we have used equation (4.7) for the radial velocity v_R . Combining the preceding expressions, the criterion for acceleration to occur before the protons are swept into the black hole becomes

$$\frac{t_{\text{shear}}}{t_{\text{infall}}} = \frac{Q(R_*)}{v_1} \left(1 - \frac{v_0}{2v_1}\right)^{-1/2} < 1, \quad (6.4)$$

where

$$Q(R_*) \equiv \frac{\alpha \gamma_0 (\gamma_0 - 1) c (R_* - 2)^2}{R_* (R_* + 2)}. \quad (6.5)$$

We treat $v_0 \equiv \xi_0 c$ as a free parameter in our model, and therefore equation (6.4) yields a constraint on the diffusion velocity in the corona, v_1 , which can be expressed as

$$v_1 > v_{\text{min}} \equiv \frac{v_0}{4} + \sqrt{\frac{v_0^2}{16} + Q^2(R_*)}. \quad (6.6)$$

It is straightforward to demonstrate that $dQ/dR_* > 0$, and therefore v_{min} increases with increasing R_* . Consequently the outermost radius of the jet, R_{out} , will correspond to the largest radius at which v_1 exceeds v_{min} . We must keep this self-consistency condition in mind when evaluating the computational results presented in § 7.

6.2. Acceleration vs. Collisional Losses

In the two-temperature disks considered here, the protons are virially hot, and they therefore collide much more frequently with kinks in the tangled magnetic field than they do with each other as shown in Paper 1. According to equation (3.1), strong proton-proton interactions are much more important than Coulomb collisions for the energetic protons in the disk and the corona. Although rare, the proton-proton collisions are usually catastrophic and typically result in the near-stopping of one of the particles. Conversely, the second-order Fermi acceleration of a proton occurs as a result of multiple collisions with magnetic scattering centers that inherit their shear motion from the underlying disk. In order for net acceleration to occur in the corona, the shear acceleration timescale expressed by equation (6.2) must not exceed the loss timescale due to proton-proton collisions calculated using equation (3.2),

$$t_{\text{loss}} \equiv -\frac{\epsilon}{\dot{\epsilon}_{\text{loss}}} = \frac{1}{\sigma_{\text{pp}} c N_1}. \quad (6.7)$$

The proton number density in the corona can be evaluated by combining equations (4.12) and (4.21), which yields

$$N_1 = \frac{\dot{M} v_0}{4 \pi R H m_p v_R v_1}. \quad (6.8)$$

Using equations (6.2), (6.7), and (6.8), the criterion for net acceleration to occur in the corona becomes

$$\frac{t_{\text{shear}}}{t_{\text{loss}}} = \frac{c \sigma_{\text{pp}} \dot{M} v_0 (R_* - 2)^2}{2 \pi m_p H v_R v_1^2 (R_* + 2) R_*^{1/2}} \left(1 - \frac{v_0}{2 v_1}\right)^{-1/2} < 1. \quad (6.9)$$

Substituting for v_R and H using equations (4.7) and (4.8), respectively, yields an expression for the maximum accretion rate as a function of radius, which can be written as

$$\frac{\dot{M}_{\text{max}}(R_*)}{\dot{M}_{\text{E}}} \equiv \frac{\alpha 5^{3/2}}{54} \frac{\sigma_{\text{T}}}{\sigma_{\text{pp}}} \frac{v_1^2}{v_0 c} \frac{R_* + 2}{R_*} \left(1 - \frac{v_0}{2 v_1}\right)^{1/2} \left(1 - \frac{2}{R_*}\right)^{-3/2}, \quad (6.10)$$

where $\dot{M}_{\text{E}} \equiv L_{\text{E}}/c^2$ is the Eddington accretion rate corresponding to the Eddington luminosity $L_{\text{E}} \equiv 4\pi GMm_p c/\sigma_{\text{T}}$. Note that the value of \dot{M}_{max} at a particular radius R_* also depends on the value of v_1 obtained at that radius. In specific applications, we generally find that $\dot{M}_{\text{max}} \gg \dot{M}_{\text{E}}$, and therefore collisional losses do not provide a very strong constraint on the model.

6.3. Pair Production in the Corona

The detailed results presented in § 7 suggest that energy losses due to strong interactions are unimportant for the protons in the corona unless the accretion rate is highly super-Eddington. We established in § 3 that losses due to strong interactions dominate over proton-proton Coulomb losses in the corona, and these in turn dominate over proton-electron Coulomb losses (Schmidt 1966), implying that proton-electron Coulomb interactions are negligible in the corona. However, this conclusion must be modified if electron-positron pair production takes place at a significant rate in the corona, because the presence of pairs can substantially reduce the timescale for the protons to cool via Coulomb coupling.

We can estimate the density of electron-positron pairs in the corona by considering the probability that a γ -ray of energy E_γ will be converted into an electron-positron pair while traversing the corona due to a collision with another (target) γ -ray. For simplicity, we assume that the target

γ -ray also has energy E_γ . The resulting self-interaction optical depth can be calculated using equation (6.4) from Becker & Kafatos (1995), which yields

$$\tau_{\gamma\gamma}(E_\gamma) = 8 \frac{m_p}{m_e} \frac{L_\gamma}{L_E} \left(\frac{h}{R_g} \right)^{-1} \left(\frac{E_\gamma}{m_e c^2} \right)^{-5} \int_0^{\beta_{\max}} \frac{\sigma_{\gamma\gamma}(\beta)}{\sigma_T} \frac{2\beta d\beta}{(1-\beta^2)^3}, \quad (6.11)$$

where h is the thickness of the corona, L_γ is the γ -ray luminosity,

$$\beta_{\max} = \left[1 - \left(\frac{E_\gamma}{m_e c^2} \right)^{-2} \right]^{1/2}, \quad (6.12)$$

and

$$\sigma_{\gamma\gamma}(\beta) = \frac{3}{16} \sigma_T (1-\beta^2) \left[(3-\beta^4) \ln \left(\frac{1+\beta}{1-\beta} \right) - 2\beta(2-\beta^2) \right]. \quad (6.13)$$

For typical γ -ray blazars, most of the observed luminosity is carried by photons with energy $E_\gamma \sim 1$ GeV, in which case we obtain

$$\tau_{\gamma\gamma} \approx 10^{-5} \frac{L_\gamma}{L_E} \left(\frac{h}{R_g} \right)^{-1}. \quad (6.14)$$

The detailed results presented in § 7 indicate that $h/R_g \sim 10$, and we therefore conclude that photon-photon pair production in the corona is unimportant for any reasonable value of L_γ . We can extend this argument to conclude that pair production via particle collisions is also insignificant. It follows that no pair-related enhancement in the proton-electron Coulomb loss rate occurs, and consequently our assumption of negligible Coulomb losses in the corona is justified.

6.4. Asymptotic Kinetic Power

We can derive another type of model constraint by computing the asymptotic kinetic power of one of the jets in comparison to the theoretical limit $(1/2) \dot{M}_{\text{out}} c^2$ for cold matter accreting from rest at infinity. At a large distance from the central mass, the internal energy of the proton distribution becomes negligible compared with the kinetic energy of the bulk motion, and the asymptotic kinetic power of one of the jets can therefore be calculated using

$$L_{\text{jet}}(R) = -c^2 \int_R^{R_{\text{out}}} \Gamma_\infty(R') \frac{d\dot{m}(R')}{dR'} dR' \sim \text{ergs s}^{-1}, \quad (6.15)$$

which sums up the contributions due to energetic protons feeding the base of the outflow between radii R and R_{out} . The negative sign arises because $d\dot{m}/dR < 0$. We can use equations (4.19) and

(4.22) to rewrite equation (6.15) as

$$L_{\text{jet}}(R) = \frac{c^2}{2\sqrt{R_g}} \left(\frac{9}{5}\right)^{3/2} \frac{\xi_0}{\alpha} \int_R^{R_{\text{out}}} \frac{\Gamma_\infty(R') \dot{M}(R')}{\sqrt{R' - 2R_g}} dR', \quad (6.16)$$

where \dot{M} is evaluated using equation (4.23).

Once a series of critical solutions has been obtained for the range of radii contained within the bounds of integration and the corresponding values of $\Gamma_\infty(R)$ have been computed using equation (5.21), equation (6.16) can be used to calculate the kinetic luminosity of the jet. Note that L_{jet} diverges as the horizon is approached ($R \rightarrow 2R_g$) because of the behavior of the denominator in equation (6.16). We can therefore establish a rough estimate for the innermost radius of the jet, R_{in} , by setting

$$L_{\text{jet}}(R_{\text{in}}) = \frac{1}{2} \dot{M}_{\text{out}} c^2. \quad (6.17)$$

In the vicinity of R_{in} , we expect the validity of our model to break down because the disk has lost virtually all of its internal energy to the wind/jet, and therefore our assumption of virial disk structure obviously becomes inconsistent. Nonetheless, the values obtained for R_{in} in specific models will provide useful insight into the radial extent of the jet. With R_{in} determined using equation (6.17), it is interesting to compute the mean asymptotic Lorentz factor of the jet by averaging $\Gamma_\infty(R)$ between R_{in} and R_{out} , weighted by the differential mass loss rate. The mean value obtained is

$$\langle \Gamma_\infty \rangle \equiv -\frac{1}{\dot{m}(R_{\text{in}})} \int_{R_{\text{in}}}^{R_{\text{out}}} \Gamma_\infty(R') \frac{d\dot{m}(R')}{dR'} dR' = \frac{1}{2} \frac{\dot{M}_{\text{out}}}{\dot{m}(R_{\text{in}})}, \quad (6.18)$$

where the final result follows from equations (6.15) and (6.17). We can substitute for $\dot{m}(R_{\text{in}})$ using equation (4.24) to obtain the equivalent result

$$\langle \Gamma_\infty \rangle = \frac{\dot{M}_{\text{out}}}{\dot{M}_{\text{out}} - \dot{M}_{\text{in}}}, \quad (6.19)$$

where $\dot{M}_{\text{in}} \equiv \dot{M}(R_{\text{in}})$ is the rate at which matter actually crosses the event horizon and enters the hole.

7. RESULTS

The rate at which the proton distribution cools and deposits its energy into the bulk motion of the plasma depends on the shape of the streamlines. As explained in § 5, we arrive at a one-dimensional problem by assuming azimuthal symmetry in the outflow and introducing the streamtube function $r \equiv f(R, z)$, which is the locus of streamlines originating at a given radius R in the corona. All of the critical point constraints described in § 5 depend on the streamtube function, which has been left unspecified up to this point. The actual shape of the streamlines may be very complicated, and there have been many attempts to understand the collimation of the flow on various scales (e.g., Blandford & Payne 1982; Contopoulos & Lovelace 1994; Lynden-Bell 1996). In view of the prevalent uncertainty, we adopt the conical outflow model utilized by Mannheim (1993) and by Blandford & Konigl (1979),

$$r = f(R, z) = R + (z - z_1) \tan \theta, \quad (7.1)$$

where θ is the half-angle of the flow.

We next discuss representative results obtained using four models constructed using two values each for the half-angle θ and the tangling parameter ξ_0 . Once the global parameters θ , $\xi_0 \equiv v_0/c$, and α are specified, we determine the critical structure of the coupled disk/corona/wind system by solving simultaneously equations (5.15), (5.16), (5.17), (5.18), (5.19), and (5.20) for the quantities $(v_1, z_1, s_1, v_c, z_c, s_c)$ as functions of the (cylindrical) starting radius in the corona R . Once the critical structure has been established, we can solve for the variation of the vertical velocity v as a function of the height z by solving equation (5.13) as discussed in § 5. We set $\alpha = 1$ in all of the models in order to simulate the effects of rapid infall between the radius of marginal stability and the event horizon. In Models 1 and 2 we set $\xi_0 = 0.05$, and in Models 3 and 4 we set $\xi_0 = 0.1$. In Models 1 and 3 we set $\theta = 0.5^\circ$, and in Models 2 and 4 we set $\theta = 1.0^\circ$. Our graphical results will be presented using a uniform set of line styles for Model 1 (*solid line*), Model 2 (*dotted line*), Model 3 (*dashed line*), and Model 4 (*dot-dashed line*). In Table 1 we summarize the results obtained in each case for the inner jet radius R_{in} , the outer jet radius R_{out} , the mean asymptotic Lorentz factor $\langle \Gamma_\infty \rangle$, and the accreted mass fraction $\dot{M}_{\text{in}}/\dot{M}_{\text{out}}$. The corresponding results obtained for the

critical parameters $(v_1, z_1, s_1, v_c, z_c, s_c)$ at the jet turn-on radius $R = R_{\text{out}}$ are presented in Table 2 for each of the models.

In Figure 3 we plot the velocity ratio $v_1/v_0 = \xi_1/\xi_0 = N_0/N_1$ (see eqs. [4.11] and [4.13]) as a function of the dimensionless cylindrical starting radius $R_* \equiv Rc^2/GM$ for each of the four models. We also plot curves corresponding to v_{min}/v_0 computed using equation (6.6). As discussed in § 6, when $v_1 < v_{\text{min}}$, protons are advected into the black hole before they can be accelerated via the Fermi process, and therefore the condition $v_1 = v_{\text{min}}$ defines the outermost radius of the jet, R_{out} (see Table 1). At radii smaller than R_{out} , acceleration dominates over advection because of the steep nature of the pseudo-Newtonian potential. The plots indicate that $N_1 < N_0$, which is reasonable since the corona is populated by protons that diffuse out of the disk. Note that the velocity ratio essentially indicates the ratio of the mean proton energies in the corona and the disk, since

$$\frac{\langle \epsilon_1 \rangle}{\langle \epsilon_0 \rangle} = \frac{1}{1-y} = 2 \frac{v_1}{v_0}, \quad (7.2)$$

which we have obtained by combining equations (3.9) and (4.16). Figure 3 therefore implies that $\langle \epsilon_1 \rangle / \langle \epsilon_0 \rangle \sim 8 - 20$ for the computed models, or, equivalently, $y \sim 0.88 - 0.95$.

In Figure 4 we depict the results obtained for the coherence length in the corona divided by the coherence length in the disk, $\tilde{\lambda}_1/\tilde{\lambda}_0$, as a function of R_* . We see that this ratio always exceeds unity in all of the plots, indicating that the field lines are less tangled in the corona than they are in the disk. This is consistent with the simulations of Romanova et al. (1998), who found that magnetic loops in the corona tend to open up due to differential rotation in the disk. In Figure 5 we plot the solutions obtained for the height of the wind-corona interface, z_1 , and for the height of the critical surface, z_c , as functions of the starting radius R_* for each model. The height of the critical surface increases with increasing radius due to the decrease in the depth of the gravitational potential at the base of the flow. Note that for a fixed value of ξ_0 , the critical surface moves away from the disk as θ decreases. In the limit of cylindrical flow ($\theta \rightarrow 0$), the critical surface is pushed out to infinity, and the flow loses its critical behavior entirely. The critical height z_c generally lies above the starting height z_1 , in which case the flow is subsonic at its base. However, the behavior

of Model 2 is reversed in the sense that the flow is already supersonic at the base (i.e., $z_c < z_1$). In this case, the critical point is virtual in nature, and does not actually exist in the flow.

In Figure 6 we plot the asymptotic Lorentz factor Γ_∞ (eq. [5.21]) as a function of R_* for each of the models. In all four cases Γ_∞ greatly exceeds unity in the inner region, indicating the formation of a relativistic jet. The asymptotic Lorentz factor tends to decrease with increasing radius due to the diminishing strength of the Keplerian shear. For a fixed value of θ , Γ_∞ tends to increase with decreasing ξ_0 , reflecting an increase in the sound speed at the base of the flow (cf. Fig. 3 and eq. [5.19]). In general, we find that $2 \lesssim \Gamma_\infty \lesssim 10$, in reasonable agreement with observations of the bulk Lorentz factors of blazar jets (e.g., Vermeulen & Cohen 1994; von Montigny et al. 1995).

In Figure 7 we use equation (4.23) to plot the radial variation of the disk accretion rate \dot{M} as a function of R_* for each of the models. The accretion rate decreases with decreasing radius in response to the loss of mass into the jet and the counterjet. The curves are normalized with respect to the accretion rate \dot{M}_{out} at the jet turn-on radius R_{out} (see Fig. 3 and Table 1), and the accreted mass fraction corresponds to $\dot{M}(R_{\text{in}})/\dot{M}_{\text{out}}$. In Figure 8 we plot the upper limit for the accretion rate, $\dot{M}_{\text{max}}(R_*)/\dot{M}_{\text{E}}$, evaluated using equation (6.10). When the actual accretion rate \dot{M} exceeds \dot{M}_{max} , losses due to proton-proton collisions in the corona dominate over Fermi energization, and the protons are decelerated rather than accelerated. It is apparent from Figure 8 that jets can exist provided $\dot{M}_{\text{out}}/\dot{M}_{\text{E}} \lesssim 10 - 20$, so that the accretion rate supplied to the outer edge of the disk is not very strongly constrained, and the accretion can be highly super-Eddington. However, for accretion rates in excess of \dot{M}_{E} , the underlying disk will cool so much that it loses its two-temperature character, resulting in the turning off of the jet (Rees et al. 1982).

In Figure 9 we use equation (6.16) to plot the asymptotic kinetic luminosity of the jet, $L_{\text{jet}}(R)$, divided by the maximum accretion luminosity $(1/2) \dot{M}_{\text{out}} c^2$. The inner radius of the jet, R_{in} , is defined as the radius at which this ratio reaches unity (see eq. [6.17] and Table 1). The estimates obtained for R_{in} in this manner are obviously quite rough, since the actual kinetic luminosity is not likely to approach $(1/2) \dot{M}_{\text{out}} c^2$.

In order to investigate the vertical structure of the flow for a particular value of the starting radius R , in Figure 10 we plot the Lorentz factor Γ computed using equation (5.7) as a function

of the height z measured from the midplane of the disk. In each case we set $R = R_{\text{out}}$ so that the results describe the outer edge of the jet. It is apparent that the flow accelerates strongly out to a distance of $\sim 10^6 R_g$ from the central mass, which corresponds to ~ 100 pc for a $10^9 M_\odot$ black hole. On the other hand, at a distance of ~ 1 pc $\sim 10^4 R_g$, the jet may very well collide with a broad-line cloud and become disrupted, resulting in the production of high-energy γ -ray emission. The asymptotic Lorentz factor Γ_∞ has not yet been achieved at this distance, but the flow is nonetheless highly relativistic ($\Gamma \gtrsim 2$), and therefore most of the energy flux (both kinetic and internal) should be converted into observable γ -rays as we discuss in § 8.

We further explore the transonic nature of the flow in Figure 11 by plotting the Mach number for the motion in the (r, z) plane,

$$\mathcal{M}_{rz} \equiv \frac{v(1 + f_z^2)^{1/2}}{a} \quad (7.3)$$

as a function of z , where a is the relativistic sound speed (see eq. [5.12]). As in Figure 10, we set $R = R_{\text{out}}$. The sonic transition occurs at $z = z_c$, where $\mathcal{M}_{rz} = 1$. Essentially all of the acceleration occurs beyond the sonic point, which acts as a “throttle” in the flow. Finally, in Figure 12 we plot curves representing the variation of the number density in the wind, N , as a function of z for $R = R_{\text{out}}$. The density declines sharply above the base of the flow at $z = z_1$, suggesting that shear (viscous) stresses will not have a strong effect on the structure of the wind/jet.

8. DISCUSSION AND CONCLUSION

We have investigated the properties of a coupled disk-corona model in which the corona joins onto a relativistic proton-electron wind, which transforms into a jet far from the central object. The expansion of the wind is powered by the pressure of the protons, which are accelerated in the corona via a second-order Fermi mechanism driven by the shear flow in the underlying accretion disk. As discussed in § 3, this mechanism preferentially accelerates high-energy protons and consequently it adds a power-law tail to the thermal proton distribution diffusing into the corona from the disk. The acceleration of the relativistic protons occurs at the expense of the azimuthal kinetic energy of the disk, and in this sense the entire process acts as a source of viscosity in the disk. This viscosity

is essentially magnetic in nature, and the dissipated energy is carried from the disk into the corona via the Poynting flux of the shearing magnetic field.

The shear-driven Fermi acceleration process transfers energy to all of the protons, whether they are located in the disk or the corona. However, the consequences of the energy transfer differ depending on the importance of proton-proton collisions, which tend to thermalize the energy. According to our results, the density in the corona is low enough to facilitate the development of a power-law tail, whereas in the disk collisional thermalization is probably efficient enough to maintain a Maxwellian proton distribution. The transfer of energy to the thermal disk protons via the Fermi acceleration process is equivalent to conventional viscous heating, and the energy therefore changes form (from kinetic to internal) but still remains in the disk.

We have chosen to focus on hot, two-temperature accretion disks around black holes in this paper because such disks are an abundant source of high-energy seed protons. Motivated by the results of MHD simulations performed by various groups, we have assumed that the corona is threaded by a tangled magnetic field which is frozen into the underlying disk. The disk structure is treated in an approximate manner by assuming a virial value for the disk energy density. The connection between the structures of the disk and the corona is established by assuming that vertically propagating sound waves enforce pressure equilibrium between the two regions. We are thus able to establish a clear link between the accretion disk and the relativistic outflow which is presumably responsible for many of the observed properties of blazars. In particular, proton-dominated jets have been invoked frequently as a likely explanation for the observed GeV and TeV emission from blazars, and this work therefore represents an important step in building a complete picture that couples the central black hole, the surrounding accretion disk, and the relativistic outflow.

The general conclusion that can be drawn from our results is that relativistic proton outflows with asymptotic Lorentz factors $\Gamma_\infty \lesssim 10$ can exist so long as the gas is supplied at a rate $\dot{M}_{\text{out}}/\dot{M}_{\text{E}} \lesssim 10 - 20$. This large upper limit implies that relativistic outflows can exist for accretion rates spanning the range from sub-Eddington to highly super-Eddington, although the existence of the underlying hot accretion disk may become questionable for substantially super-

Eddington accretion rates due to efficient bremsstrahlung cooling. The values we obtain for the asymptotic Lorentz factor are consistent with those implied by observations of blazars (Vermeulen & Cohen 1994; von Montigny et al. 1995), although it is not clear that the flows considered here actually achieve the asymptotic Lorentz factor, since this may require the jet to remain intact up to 10 kpc from the central object.

8.1. *Production of Radiation in Jet-Cloud Collisions*

Given the uncertainty in the geometry of the jet, the actual division of energy between internal and kinetic forms that characterizes the jet at the time it collides with target protons in a broad-line emission cloud is unclear. It is therefore difficult to predict the detailed spectrum of the emergent γ -radiation for this process. However, the asymptotic Lorentz factor of the jet provides some overall indications. Let us assume for example that the jet has $\Gamma_\infty \sim 10$, and that it is intercepted by a broad-line emission cloud after it has achieved its asymptotic Lorentz factor. The average energy of the emergent radiation in a proton-proton reaction is $\sim 0.1 \times 0.5$ times the energy of the incident high-energy proton involved in the reaction (Katz 1991). The factor of 0.1 expresses the overall efficiency of the cascade process, and the factor of 0.5 appears because two photons will emerge from a reaction initiated by a single proton. Since the total energy carried by a cold proton moving with $\Gamma_\infty \sim 10$ is ~ 10 GeV, we conclude that radiation from the process described above will be centered around 0.5 GeV, and that the total luminosity of the radiation will be $\sim 5\%$ of the asymptotic kinetic power of the jet. If the asymptotic Lorentz factor has not been achieved by the time the jet collides with the cloud, then a significant fraction of the jet luminosity is still carried in the form of advected internal energy. However, the results are not likely to be very different in this case since the total power of the jet is nearly equal to the asymptotic power at large distances from the black hole.

We can estimate the kinetic jet luminosity required to power an observed flux of γ -rays by employing a simple model for the emission geometry describing the angular distribution of the radiation produced in the cascade. When a conical jet of the type considered in § 7 collides with a broad-line cloud, we expect the cascade radiation to be emitted in a conical distribution with an

opening angle Φ given roughly by

$$\Phi \approx \theta + \langle \Gamma_\infty \rangle^{-1}. \quad (8.1)$$

The flux of the observed γ -radiation is related to the γ -ray luminosity by

$$F_{\text{rad}} = \frac{L_{\text{rad}}}{\Omega \mathcal{L}^2}, \quad (8.2)$$

where \mathcal{L} is the distance from the observer to the source and Ω is the solid angle covered by the emitted radiation. For small values of Φ , we have $\Omega \approx \pi \Phi^2$, and equations (8.1) and (8.2) can therefore be combined to obtain

$$L_{\text{rad}} \approx \pi \mathcal{L}^2 F_{\text{rad}} (\theta + \langle \Gamma_\infty \rangle^{-1})^2. \quad (8.3)$$

In the case of the June 1993 flare of 3C 279 observed by *EGRET* on the *Compton Gamma-Ray Observatory*, we can use $\mathcal{L} = 5.65 \times 10^{27}$ cm and $F_{\text{rad}} = 2.49 \times 10^{-9}$ ergs sec $^{-1}$ cm $^{-2}$ (Becker and Kafatos 1995; Hartman 1992) along with the results for $\langle \Gamma_\infty \rangle$ in Table 1 to obtain $L_{\text{rad}}/10^{46}$ ergs s $^{-1} \approx 0.73, 0.88, 1.40,$ and 1.70 for Models 1, 2, 3, and 4, respectively. The corresponding values for the kinetic luminosity of the jet are $L_{\text{jet}}/10^{47}$ ergs s $^{-1} \approx 1.47, 1.76, 2.80,$ and $3.40,$ respectively, computed by setting $L_{\text{rad}} = 0.05 L_{\text{jet}}$. These results for L_{jet} are comparable to the Eddington luminosity for a $10^9 M_\odot$ black hole. Beall & Bednarek (1999) have recently considered a model in which a proton beam produces γ -rays upon collision with a broad-line cloud via pion production. The protons in their jet model have a power-law spectrum with an index that is set arbitrarily. Within the context of our model, the power-law index can be calculated using equation (3.14), and therefore a unified description of the jet can be constructed that connects the acceleration in the corona with the ultimate production of the γ -rays.

8.2. Shear Acceleration vs. Stochastic Acceleration

We have demonstrated that collisions with cold magnetic scattering centers embedded in a Keplerian shear flow provide an acceleration mechanism for the protons that is formally equivalent to a second-order Fermi process. However, in reality the scattering centers will be propagating MHD waves rather than cold kinks. The wave aspect imparts a *stochastic* component of motion

to the scattering centers, which will tend to augment the particle acceleration associated with their shear motion. It is therefore important to determine which mechanism dominates in a typical situation. The relative strengths of the two processes can be estimated by comparing their respective acceleration rates.

The stochastic motion of the waves will energize the protons via second-order Fermi acceleration, and in this sense it is similar to the shear acceleration mechanism. The stochastic process can therefore also be modeled using equation (2.2), and the mean acceleration rate is consequently given by equation (2.5),

$$\langle \dot{\epsilon}_{\text{stoch}} \rangle = \frac{1}{\epsilon^2} \frac{d}{d\epsilon} (\epsilon^2 \mathcal{D}_{\text{stoch}}), \quad (8.4)$$

where $\mathcal{D}_{\text{stoch}}$ is the energy diffusion coefficient for the stochastic acceleration process. The spatial diffusion coefficient in the corona, κ_1 , is related to $\mathcal{D}_{\text{stoch}}$ via (e.g., Becker, Kafatos, & Maisack 1994)

$$\kappa_1 \mathcal{D}_{\text{stoch}} = \frac{v_A^2 \epsilon^2}{9}, \quad (8.5)$$

where $v_A = B_1 / \sqrt{4\pi\rho_1}$ is the Alfvén velocity in the corona associated with magnetic field strength B_1 and density ρ_1 . Combining equations (8.4) and (8.5) and substituting for κ_1 using equation (3.6) yields

$$\langle \dot{\epsilon}_{\text{stoch}} \rangle = \frac{B_1^2 \epsilon}{3 \pi c \rho_1 \tilde{\lambda}_1}, \quad (8.6)$$

where we have assumed that κ_1 is independent of ϵ . Defining B_0 as the magnetic field strength in the disk and using equation (4.1), we obtain

$$\langle \dot{\epsilon}_{\text{stoch}} \rangle = \frac{4}{3} \left(\frac{B_1}{B_0} \right)^2 \frac{\rho_0}{\rho_1} \frac{c \epsilon}{\beta_0 \tilde{\lambda}_1} \frac{1}{R_* - 2}, \quad (8.7)$$

where $\beta_0 \equiv 8\pi U_0 / B_0^2$ is the plasma β -parameter in the disk.

We can now evaluate the ratio of the shear and stochastic acceleration rates by combining equations (2.5), (4.17), (4.18), and (8.7), which yields

$$\frac{\langle \dot{\epsilon}_{\text{shear}} \rangle}{\langle \dot{\epsilon}_{\text{stoch}} \rangle} = \frac{3}{4} \left(\frac{v_0}{c} \right)^2 \left(\frac{B_0}{B_1} \right)^2 \beta_0 (R_* - 2) \left(\frac{v_1}{v_0} - \frac{1}{2} \right). \quad (8.8)$$

Simulations of MHD dynamos driven by turbulence in accretion disks suggest that the strength of the magnetic field in the saturated state corresponds to $\beta_0 \sim 100$ (e.g., Hawley, Gammie, & Balbus 1995, Brandenburg et al. 1995). We adopt this value in Figure 13, where we use equation (8.8) to plot the ratio $\langle \dot{\epsilon}_{\text{shear}} \rangle / \langle \dot{\epsilon}_{\text{stoch}} \rangle$ as a function of the dimensionless starting radius in the corona R_* for each of the four models considered in § 7. We expect that $B_0 \gtrsim B_1$ since the field is generated by the shear in the disk. However, in order to obtain a conservative estimate, we set $B_0 = B_1$ when performing the calculations plotted in Figure 13. Note that the shear acceleration rate greatly exceeds that due to the stochastic wave motion at all radii, and consequently we have not committed a serious error by neglecting the latter process in our analysis of the particle acceleration occurring in the corona.

We have shown that the relativistic protons in the corona experience negligible losses due to collisions with other protons. However, the coronal protons also cool via the excitation of MHD waves which are amplified as a consequence of the super-Alfvénic motion of the protons along the field lines. If this cooling mechanism imposes losses comparable to the rate of shear-driven Fermi acceleration, then the net acceleration rate will be substantially lower than the value used in our model. This possibility can be ruled out by carefully considering the rates for the various energy transfer processes as follows. In a saturated steady state, the rate at which the waves transfer energy to the protons via stochastic acceleration is equal to the rate at which the protons transfer energy to the waves via the excitation process *plus* a portion of the Poynting flux from the disk (the remainder of the Poynting flux generates the shear motion of the waves). This implies that the rate at which the protons lose energy due to wave excitation is less than the rate at which the protons gain energy from the waves via stochastic acceleration. According to Figure 13, the latter process is negligible compared with the shear-driven Fermi acceleration rate, and therefore it follows that the cooling of the protons via the excitation of MHD waves is also insignificant compared with the rate of shear acceleration as we have assumed.

8.3. Conclusion

In this paper we have demonstrated the plausibility of the production of relativistic jets as a

direct consequence of the accretion of material onto a supermassive black hole. The asymptotic bulk Lorentz factors obtained in our models are commensurate with those inferred from observations of superluminal motion in blazars (Vermeulen & Cohen 1994). Having demonstrated the basic framework, it is now possible to build detailed models that can predict both the spectrum and the bulk Lorentz factor of the energetic proton population in the jet at an arbitrary distance from the central object. This information can then be used as input to detailed calculations of proton-initiated reaction cascades that ultimately result in observable high-energy emission.

Although we have focused on hot, two-temperature accretion disks as the source of particles and energy for the jet in this paper, the relativistic wind formalism developed in § 5 is not specific to the disk model used here. Advection-dominated accretion flows (Narayan & Yi 1995) represent another interesting alternative, since these flows have the attractive properties of being hot and tenuous, and may prove to be natural environments for the shear acceleration mechanism studied here. Blandford & Begelman (1999) have outlined a generalization of the advection-dominated model that includes outflows which carry away some of the binding energy of the infalling plasma. Such outflows alleviate the problem of the accreting gas having a net positive energy and therefore being gravitationally unbound, although no mechanism for generating the outflows is specified by the authors. It is conceivable that the shear acceleration mechanism described in this work could power the outflows.

The protons in the jet are expected to drag electrons along with them via Coulomb coupling, but we do not expect the inertia of the electrons to load down the jet to any appreciable extent because the electrons are much less massive than the protons. However, the cooling of the electrons via synchrotron and inverse-Compton radiation presents a potentially more serious problem, since this may lead to the cooling of the protons which would tend to quench the expansion. The adiabatic losses considered in our model take place over a sound crossing timescale, which is roughly equal to the dynamical timescale. The dynamical timescale is in turn expected to be far smaller than the electron-ion Coulomb coupling timescale since the density drops very rapidly above the disk (see Fig. 12). Hence it is not likely that electron-ion coupling will be able to cool the protons substantially before the jet has expanded to the point where the electrons and protons

have essentially stopped interacting. This may lead to the development of a charge separation in the jet. We also note that a more efficient form of electron-ion coupling may occur as a result of collective modes (Begelman & Chiueh 1988).

Strictly speaking, the distribution function and the bulk Lorentz factor Γ should be determined self-consistently along with the flow velocity, and this is the approach taken by Contopoulos & Kazanas (1995). In such a treatment, the adiabatic index of the wind cannot be regarded as a constant, and must be calculated at every spatial location. It typically varies from $4/3$ for the highly relativistic gas at the base of the outflow up to $5/3$ for the cold, nonrelativistic gas at large distances from the central object. Here we have chosen to avoid the complexity of dealing with a variable adiabatic index, and instead we have used the corona value $\gamma_1 = 4/3$ to describe the thermodynamics throughout the entire wind. The validity of this procedure can be evaluated a posteriori by using the comoving energy spectrum of the protons to recalculate the adiabatic index. We plan to compute the comoving proton distribution and the detailed γ -ray spectrum resulting from a jet-cloud collision in a later paper.

We would like to thank Professor Menas Kafatos for numerous insightful discussions throughout the development of this work.

APPENDIX A

CALCULATION OF THE MEAN ACCELERATION RATE

In this section we establish that the mean shear acceleration rate for particles with energy ϵ associated with the transport equation

$$\frac{\partial f}{\partial t} = -\frac{1}{\epsilon^2} \frac{\partial}{\partial \epsilon} \left(-\epsilon^2 \mathcal{D} \frac{\partial f}{\partial \epsilon} \right) \quad (\text{A1})$$

is given by

$$\langle \dot{\epsilon} \rangle_{\text{shear}} = \frac{1}{\epsilon^2} \frac{d}{d\epsilon} (\epsilon^2 \mathcal{D}), \quad (\text{A2})$$

as quoted in § 2. We begin by defining the energy density

$$U(t) = \int_0^\infty \epsilon^3 f(\epsilon, t) d\epsilon \sim \text{ergs cm}^{-3}, \quad (\text{A3})$$

and the number density

$$N(t) = \int_0^\infty \epsilon^2 f(\epsilon, t) d\epsilon \sim \text{cm}^{-3}. \quad (\text{A4})$$

Note the arguments made following equation (2.4) in reference to the lower bounds of the integrals in equations (A3) and (A4). Defining the average energy per particle as

$$\langle \epsilon \rangle = \frac{U}{N}, \quad (\text{A5})$$

we find that the rate of change of $\langle \epsilon \rangle$ is given by

$$\frac{d}{dt} \langle \epsilon \rangle = \frac{N dU/dt - U dN/dt}{N^2}. \quad (\text{A6})$$

Let us focus on the evolution of J particles per unit volume all having energy $\epsilon = \epsilon_i$ at time $t = t_i$.

If $f(\epsilon, t)$ denotes their distribution, then at time $t = t_i$ we have

$$f(\epsilon, t) \Big|_{t=t_i} = \frac{J}{\epsilon_i^2} \delta(\epsilon - \epsilon_i), \quad (\text{A7})$$

so that the particle number density computed using equation (A4) is J as required. We can combine equation (A4) with the kinetic equation (A1) to write the rate of change of the number density as

$$\frac{dN}{dt} = \int_0^\infty \epsilon^2 \frac{\partial f}{\partial t} d\epsilon = \int_0^\infty \frac{\partial}{\partial \epsilon} \left(\epsilon^2 \mathcal{D} \frac{\partial f}{\partial \epsilon} \right) d\epsilon. \quad (\text{A8})$$

At time $t = t_i$, the initial condition given by equation (A7) can be employed to obtain

$$\left. \frac{dN}{dt} \right|_{t=t_i} = \lim_{t \rightarrow t_i} \epsilon^2 \mathcal{D} \frac{\partial}{\partial \epsilon} f(\epsilon, t) \Big|_0^\infty = 0, \quad (\text{A9})$$

so that there is no instantaneous change in the particle number density. The analog of equation (A8) for the energy density U is

$$\frac{dU}{dt} = \int_0^\infty \epsilon^3 \frac{\partial f}{\partial t} d\epsilon = \int_0^\infty \epsilon \frac{\partial}{\partial \epsilon} \left(\epsilon^2 \mathcal{D} \frac{\partial f}{\partial \epsilon} \right) d\epsilon. \quad (\text{A10})$$

Integrating by parts twice yields

$$\frac{dU}{dt} = \epsilon^3 \mathcal{D} \frac{\partial f}{\partial \epsilon} \Big|_0^\infty - \epsilon^2 \mathcal{D} f \Big|_0^\infty + \int_0^\infty \frac{\partial}{\partial \epsilon} (\epsilon^2 \mathcal{D}) f d\epsilon, \quad (\text{A11})$$

or, incorporating the initial condition given by equation (A7),

$$\left. \frac{dU}{dt} \right|_{t=t_i} = \left. \frac{J}{\epsilon^2} \frac{\partial}{\partial \epsilon} (\epsilon^2 \mathcal{D}) \right|_{\epsilon=\epsilon_i}. \quad (\text{A12})$$

Combining equations (A6), (A9), and (A12), we arrive at

$$\left. \frac{d\langle \epsilon \rangle}{dt} \right|_{t=t_i} = \left. \frac{1}{\epsilon^2} \frac{\partial}{\partial \epsilon} (\epsilon^2 \mathcal{D}) \right|_{\epsilon=\epsilon_i}. \quad (\text{A13})$$

Although we have treated particles with energy $\epsilon = \epsilon_i$ at time $t = t_i$, the result is valid for particles with any chosen energy at any time, so that we obtain

$$\frac{d\langle \epsilon \rangle}{dt} = \frac{1}{\epsilon^2} \frac{\partial}{\partial \epsilon} (\epsilon^2 \mathcal{D}) \quad (\text{A14})$$

for the mean shear acceleration rate, in agreement with equation (A2).

REFERENCES

- Beall, J. H., & Bednarek, W. 1999, ApJ, submitted
- Becker, P. A., & Kafatos, M. 1995, ApJ, 453, 83
- Becker, P. A., Kafatos, M., & Maisack, M. 1994, ApJ Supplement, 90, 949
- Begelman, M. C. 1998, ApJ, 493, 291
- Begelman, M. C., & Chiueh, T. 1988, ApJ, 332, 872
- Blandford, R. D., & Begelman, M. C. 1999, MNRAS, submitted
- Blandford, R. D., & Konigl, A. 1979, ApJ, 232, 34
- Blandford, R. D., & Payne, D. G. 1982, MNRAS, 199, 903
- Bondi, H. 1952, MNRAS, 112, 195
- Brandenburg, A., Nordlund, A., Stein, R. F., Torkelsson, U. 1995, ApJ, 446, 741
- Chakrabarti, S. K. 1985, ApJ, 288, 1
- Contopoulos, J. 1995, ApJ, 446, 67
- Contopoulos, J., & Kazanas, D. 1995, ApJ, 441, 521
- Contopoulos, J., & Lovelace, R. V. E. 1994, ApJ, 429, 139
- Daly, R. A., & Marscher, A. P. 1988, ApJ, 334, 539
- Dar, A., & Laor, A. 1997, ApJ 478, L5
- Dermer, C. D., Miller, J. A., & Li, H. 1996, ApJ 456, 106
- Dermer, C. D & Schlickeiser, R. 1992, Science, 257, 1642
- Earl, J. A., Jokipii, J. R., & Morfill, G. 1988, ApJ, 331, L91
- Eilek, J. A., & Kafatos, M. 1983, ApJ, 271, 804
- Frank, J., King, A. R., & Raine, D. J. 1992, *Accretion Power in Astrophysics* (Cambridge: Cambridge University Press)
- Hartman, R. C., et al. 1992, ApJ, 385, L1
- Hawley, J. F., Gammie, C. F., Balbus, S. A. 1995, ApJ, 440, 742
- Katz, J. I. 1991, ApJ, 367, 407
- Kazanas, D., & Ellison, D. C. 1986, ApJ, 304, 178
- Landau, L. D., & Lifshitz, E. M. 1987, *Fluid Mechanics* (New York: Pergamon Press)

- Li, Z.-Y., Chiueh, T., & Begelman, M. C. 1992, *ApJ*, 394, 459
- Lynden-Bell, D. 1996, *MNRAS*, 279, 389
- Mannheim, K. 1993, *A & A*, 269, 67
- Mastichiadis, A., & Kazanas, D. 1993, *BAAS*, 182, 12.07
- Matsumoto, R., & Tajima, T. 1995, *ApJ*, 445, 767
- Mészáros, P., & Rees, M. J. 1992, *MNRAS*, 257, 29
- Mihalas, D., & Mihalas, B. W. 1984, *Foundations of Radiation Hydrodynamics* (New York: Oxford University Press)
- Narayan, R., & Yi, I. 1995, *ApJ*, 444, 231
- Paczynski, B., & Wiita, P. J. 1980, *A & A*, 88, 23
- Phinney, E. S. 1982, *MNRAS*, 198, 1109
- Protheroe, R. J., & Kazanas, D. 1983, *ApJ*, 265, 620
- Rees, M. J., Begelman, M. C., Blandford, R. D., & Phinney, E. S. 1982, *Nature*, 295, 17
- Reif, F. 1965, *Fundamentals of Statistical and Thermal Physics* (New York: McGraw-Hill)
- Romanova, M. M., Ustyugova, G. V., Koldoba, A. V., Chechetkin, V. M., & Lovelace, R. V. E. 1998, *ApJ*, 500, 703
- Rybicki, G. B., & Lightman, A. P. 1979, *Radiative Processes in Astrophysics* (New York: Wiley)
- Shapiro, S. L., Lightman, A. L., & Eardley, D. M. 1976, *ApJ*, 204, 187
- Schmidt, G. 1966, *Physics of High Temperature Plasmas* (New York: Academic)
- Subramanian, P. 1997, PhD Thesis, George Mason University
- Subramanian, P., Becker, P. A., & Kafatos, M. 1996, *ApJ*, 469, 784 (Paper 1)
- Ustyugova, G. V., Koldoba, A. V., Romanova, M. M., Chechetkin, V. M., & Lovelace, R. V. E. 1995, *ApJ*, 439, L39
- Webb, G. M., Jokipii, J. R., & Morfill, G. E. 1994, *ApJ*, 424, 158
- Wehrle, A. E. et al. 1998, *ApJ*, 497, 178
- Weinberg, S. 1972, *Gravitation and Cosmology: Principles and Application of the General Theory of Relativity* (New York: Wiley)
- Vermeulen, R. C., & Cohen, M. H. 1994, *ApJ*, 430, 467
- von Montigny, C. et al. 1995, *ApJ*, 440, 525

TABLE 1

Global Model Parameters

Model	θ	ξ_0	R_{in}/R_g	R_{out}/R_g	$\langle \Gamma_\infty \rangle$	$\dot{M}_{\text{in}}/\dot{M}_{\text{out}}$
1	0.5°	0.05	4.47	7.37	6.076	0.835
2	1.0°	0.05	4.95	8.28	5.765	0.826
3	0.5°	0.1	3.55	5.25	4.244	0.764
4	1.0°	0.1	3.91	5.97	3.929	0.745

TABLE 2

Model Parameters for $R = R_{\text{out}}$

Model	z_1/R_g	v_1/c	s_1/c	z_c/R_g	v_c/c	s_c/c	Γ_∞
1	20.9	0.48	0.89	22.8	0.48	0.89	4.24
2	26.9	0.53	0.86	16.5	0.48	0.88	4.16
3	9.2	0.33	0.68	22.5	0.43	0.64	2.96
4	12.6	0.39	0.66	17.6	0.43	0.65	2.88

FIGURE CAPTIONS

Fig. 1. – Schematic depiction of second-order Fermi acceleration resulting from an average collision between a proton originating at the (stationary) origin and a scattering center (cold magnetic kink) located in one of the four quadrants. The solid circle at the center represents the incident proton, and the open circles in the four quadrants represent the scattering centers, which move with the velocity of the shear flow.

Fig. 2. – Schematic diagram of the disk/corona/wind geometry.

Fig. 3. – Comparison of v_1/v_0 and v_{\min}/v_0 as functions of the dimensionless cylindrical starting radius in the corona, R_* , for each of the computed models. The point of intersection of these two curves defines the outer radius (see eq. [6.6]). The thin lines represent v_1/v_0 and the heavy lines represent v_{\min}/v_0 . Throughout the results presented here, we will use a uniform set of line styles for Model 1 (*solid lines*), Model 2 (*dotted lines*), Model 3 (*dashed lines*), and Model 4 (*dash-dot lines*).

Fig. 4. – Ratio of magnetic coherence lengths in the corona and disk, $\tilde{\lambda}_1/\tilde{\lambda}_0$, plotted as a function of the dimensionless starting radius R_* for each of the computed models. In each case the field lines are less tangled in the corona than they are in the disk.

Fig. 5. – Comparison of the height of the critical surface z_c and the starting height for the wind z_1 as functions of the dimensionless starting radius R_* for each of the models. The thin lines represent z_c/R_g and the heavy lines represent z_1/R_g . Note that in the case of Model 2 the wind is supersonic at the base. In all of the other cases, the wind is subsonic at the base.

Fig. 6. – Asymptotic Lorentz factor Γ_∞ plotted as a function of the starting radius R_* using eq. (5.21). For all of the models, the asymptotic Lorentz factor tends to decrease with increasing radius due to the diminishing strength of the Keplerian shear.

Fig. 7. – Radial variation of the disk accretion rate \dot{M} as a function of R_* plotted using eq. (4.23) for each of the models. The accretion rate decreases with increasing radius in response

to the mass lost into the jet and the counterjet.

Fig. 8. – Upper limit on the accretion rate $\dot{M}_{\text{max}}/\dot{M}_{\text{E}}$ plotted as a function of R_* using eq. (6.10) for each of the models. For accretion rates exceeding \dot{M}_{max} , losses due to strong proton-proton collisions in the corona overwhelm the shear acceleration.

Fig. 9. – Asymptotic kinetic luminosity of the jet L_{jet} (eq. [6.16]) plotted in units of the maximum accretion luminosity $(1/2)\dot{M}_{\text{out}}c^2$ as a function of R_* . The inner radius of the jet, R_{in} , is defined as the radius at which this quantity reaches unity (see Table 1).

Fig. 10. – Lorentz factor Γ (eq. [5.7]) plotted as a function of the height z/R_g measured from the midplane of the disk for starting radius $R = R_{\text{out}}$. Note that the flow continues to accelerate at large distances from the black hole.

Fig. 11. – Mach number in the (r, z) plane, $\mathcal{M}_{r,z}$, plotted as a function of the height z/R_g above the midplane of the disk using eq. (7.3) for starting radius $R = R_{\text{out}}$.

Fig. 12. – Variation of the number density in the wind N plotted as a function of the height z/R_g above the disk midplane for starting radius $R = R_{\text{out}}$.

Fig. 13. – Ratio of the shear acceleration rate $\langle \dot{\epsilon}_{\text{shear}} \rangle$ to the stochastic acceleration rate $\langle \dot{\epsilon}_{\text{stoch}} \rangle$ plotted as a function of R_* , evaluated using eq. (8.8). Note that $\langle \dot{\epsilon}_{\text{shear}} \rangle$ greatly exceeds $\langle \dot{\epsilon}_{\text{stoch}} \rangle$ at all radii.

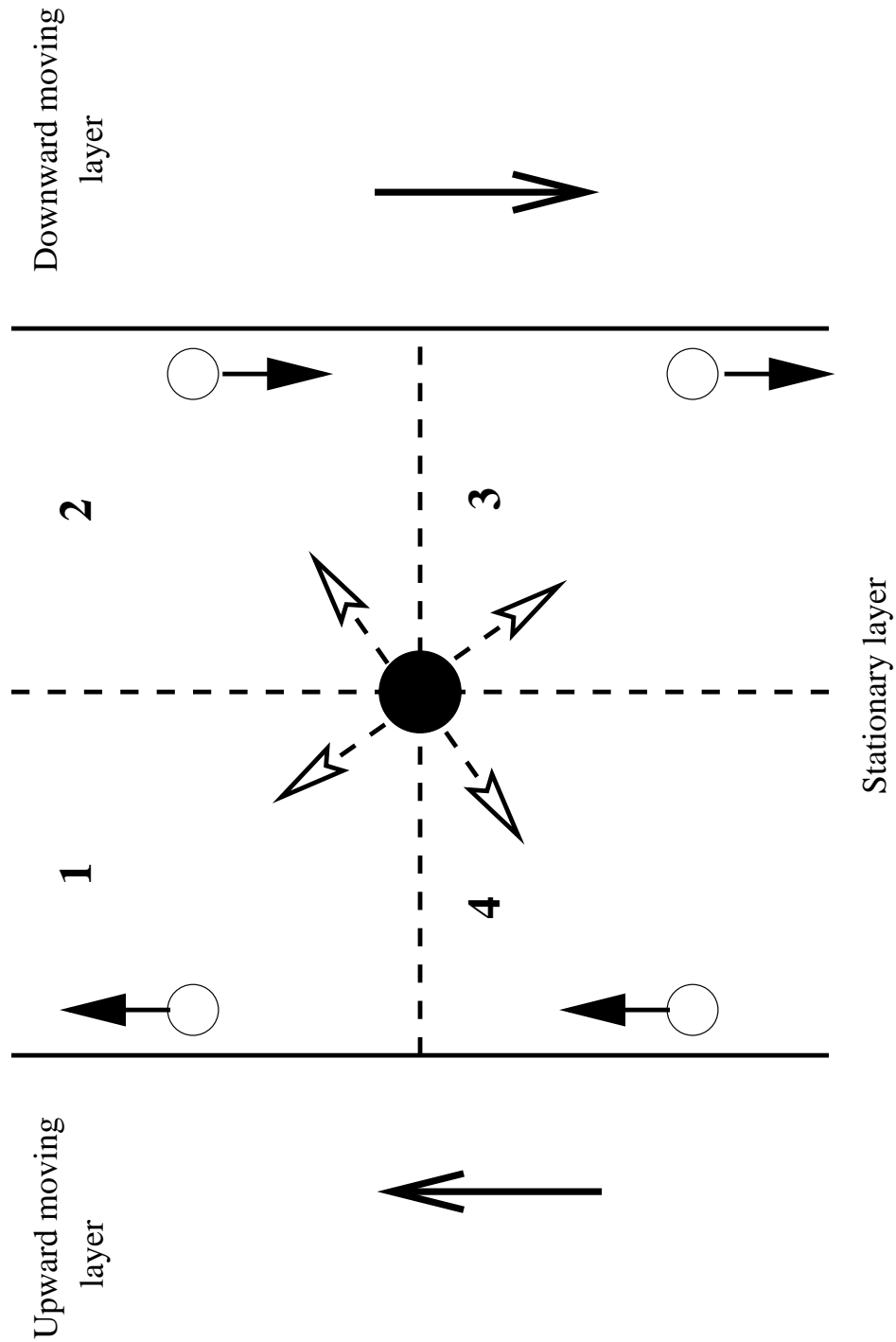
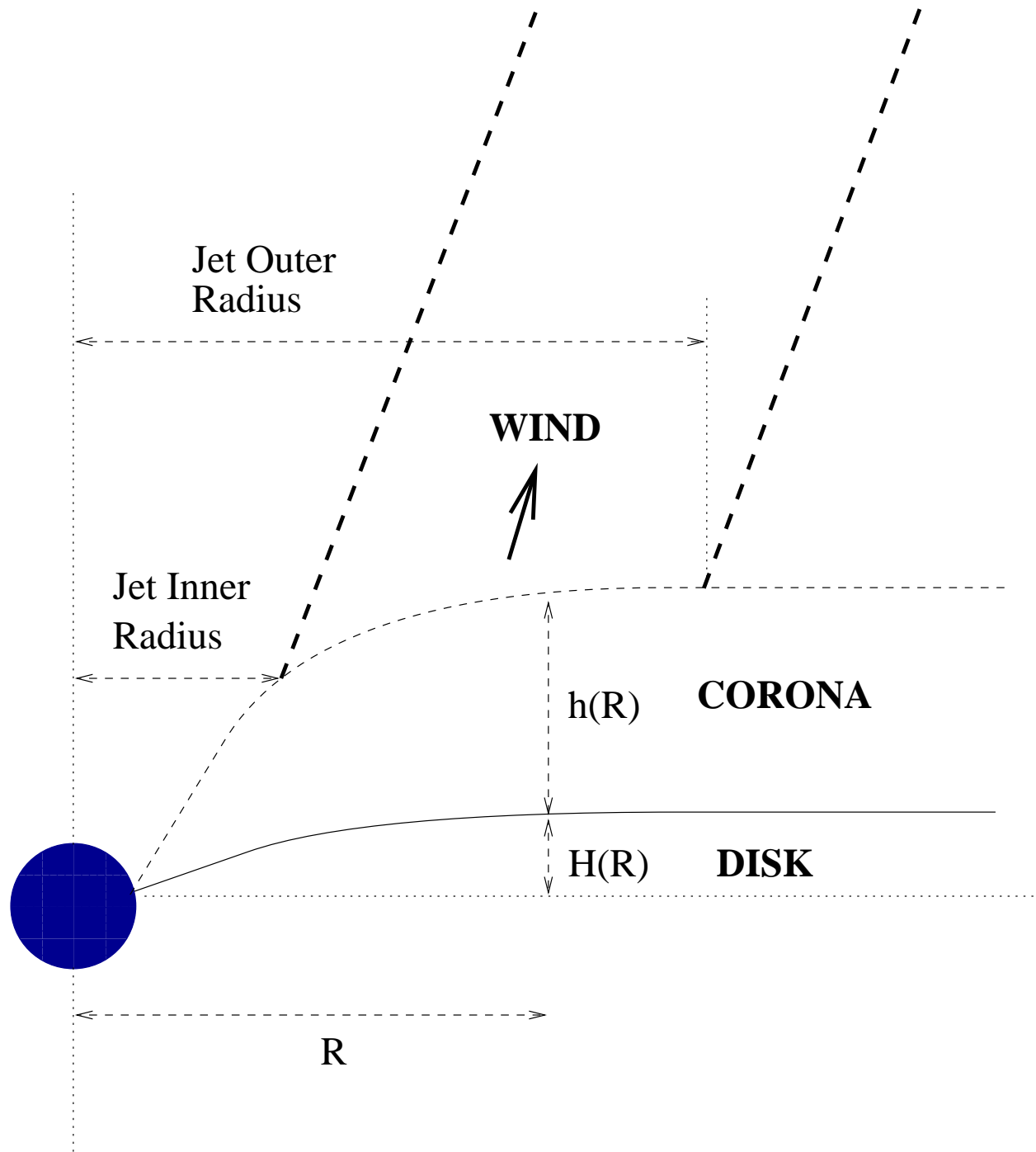


Figure 1: Schematic depiction of second-order Fermi acceleration resulting from an average collision between a proton originating at the (stationary) origin and a scattering center (cold magnetic kink) located in one of the four quadrants. The solid circle at the center represents the incident proton, and the open circles in the four quadrants represent the scattering centers, which move with the velocity of the shear flow.

Figure 2: Schematic diagram of the disk/corona/wind geometry.



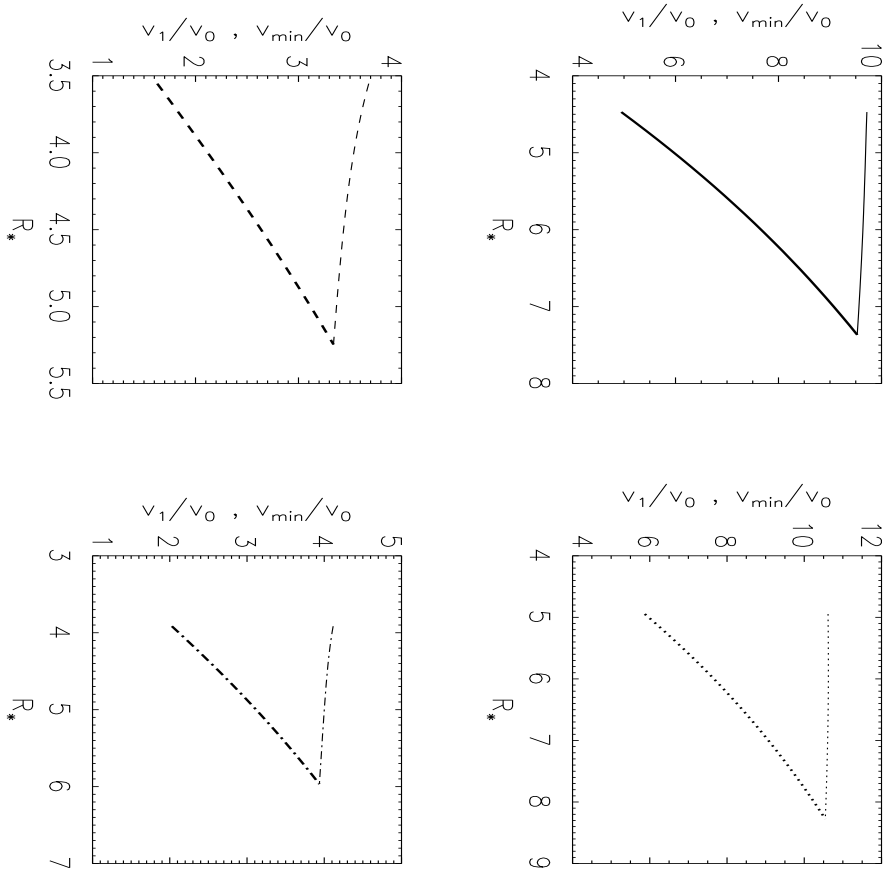


Figure 3: Comparison of v_1/v_0 and v_{\min}/v_0 as functions of the dimensionless cylindrical starting radius in the corona, R_* , for each of the computed models. The point of intersection of these two curves defines the outer radius (see eq. [6.6]). The thin lines represent v_1/v_0 and the heavy lines represent v_{\min}/v_0 . Throughout the results presented here, we will use a uniform set of line styles for Model 1 (*solid lines*), Model 2 (*dotted lines*), Model 3 (*dashed lines*), and Model 4 (*dash-dot lines*).

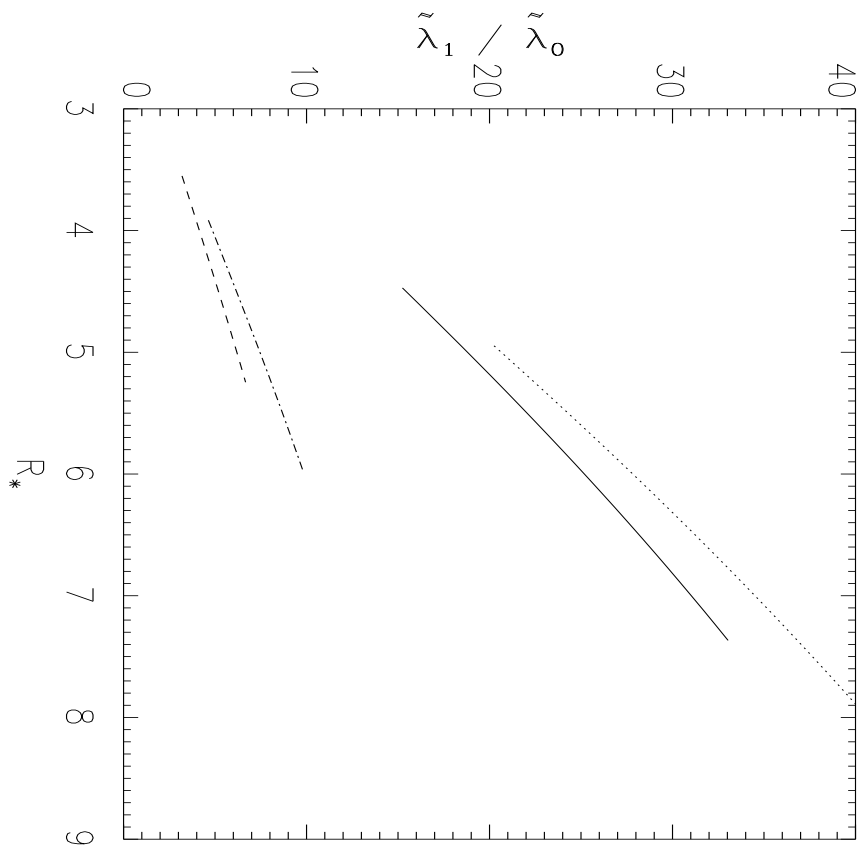


Figure 4: Ratio of magnetic coherence lengths in the corona and disk, $\tilde{\lambda}_1/\tilde{\lambda}_0$, plotted as a function of the dimensionless starting radius R_* for each of the computed models. In each case the field lines are less tangled in the corona than they are in the disk.

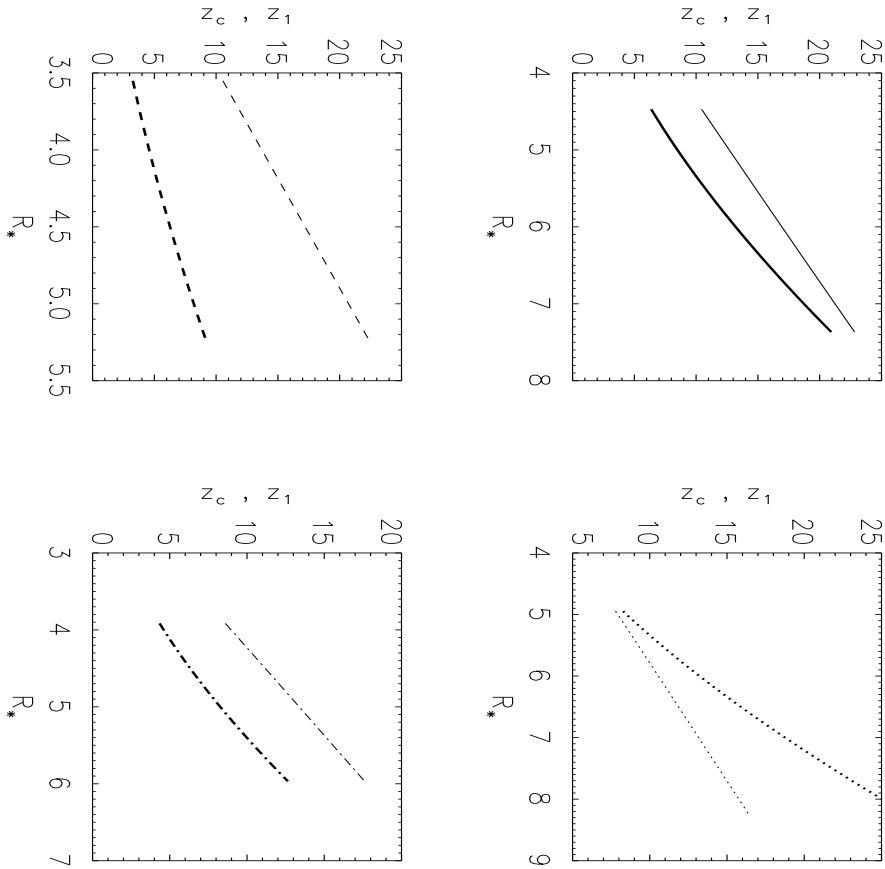


Figure 5: Comparison of the height of the critical surface z_c and the starting height for the wind z_1 as functions of the dimensionless starting radius R_* for each of the models. The thin lines represent z_c/R_g and the heavy lines represent z_1/R_g . Note that in the case of Model 2 the wind is supersonic at the base. In all of the other cases, the wind is subsonic at the base.

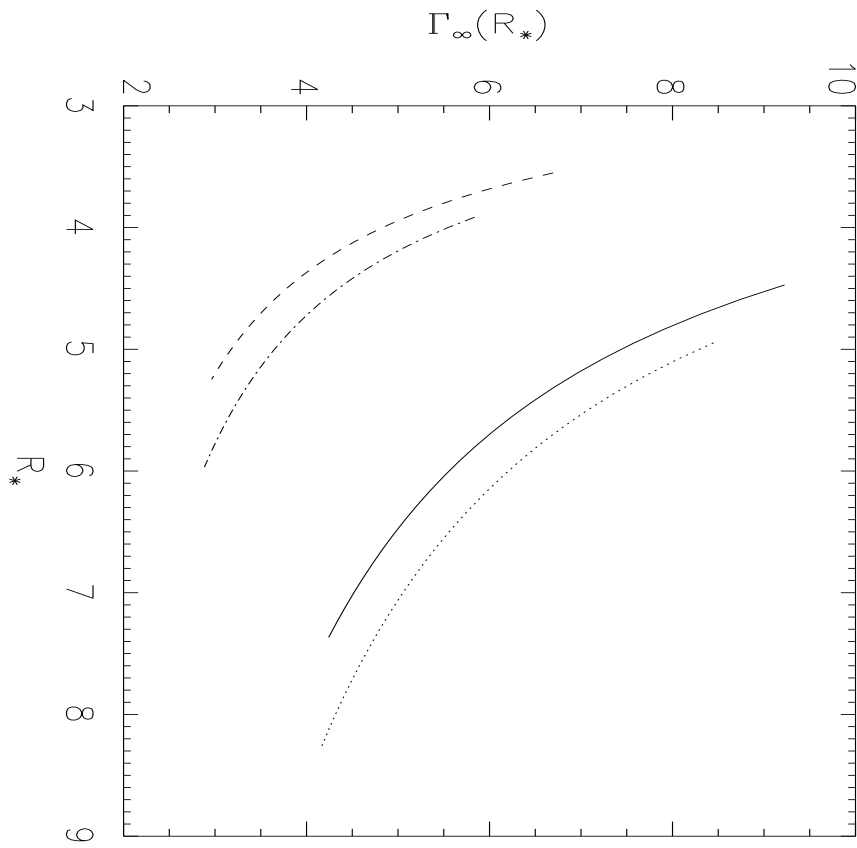


Figure 6: Asymptotic Lorentz factor Γ_∞ plotted as a function of the starting radius R_* using eq. (5.21). For all of the models, the asymptotic Lorentz factor tends to decrease with increasing radius due to the diminishing strength of the Keplerian shear.

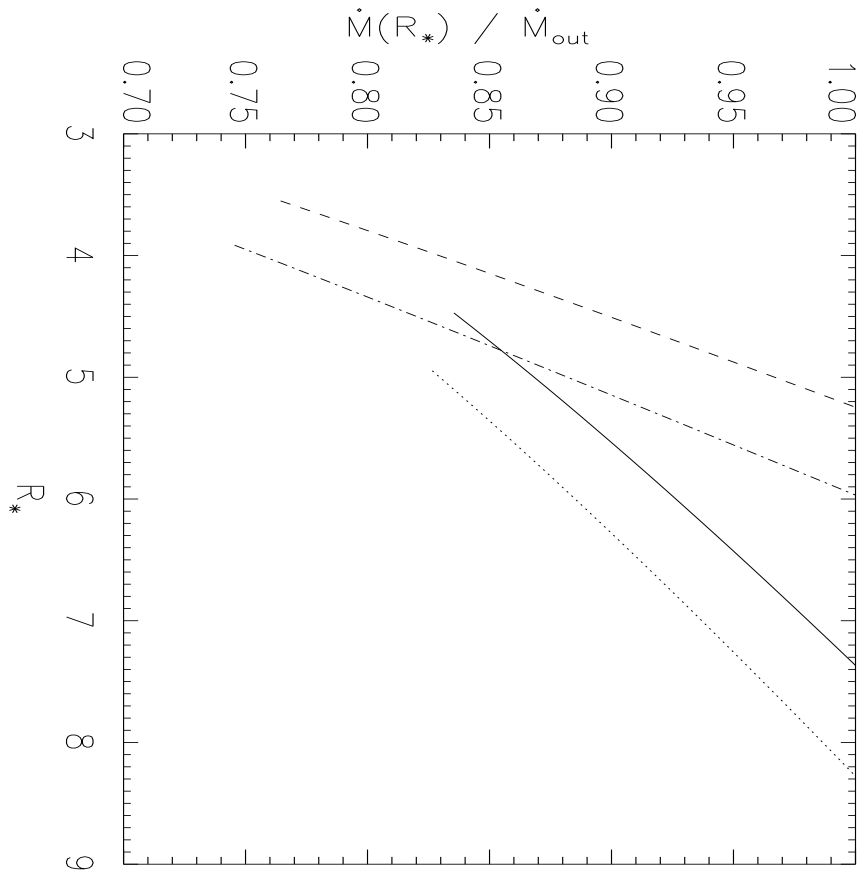


Figure 7: Radial variation of the disk accretion rate \dot{M} as a function of R_* plotted using eq. (4.23) for each of the models. The accretion rate decreases with increasing radius in response to the mass lost into the jet and the counterjet.

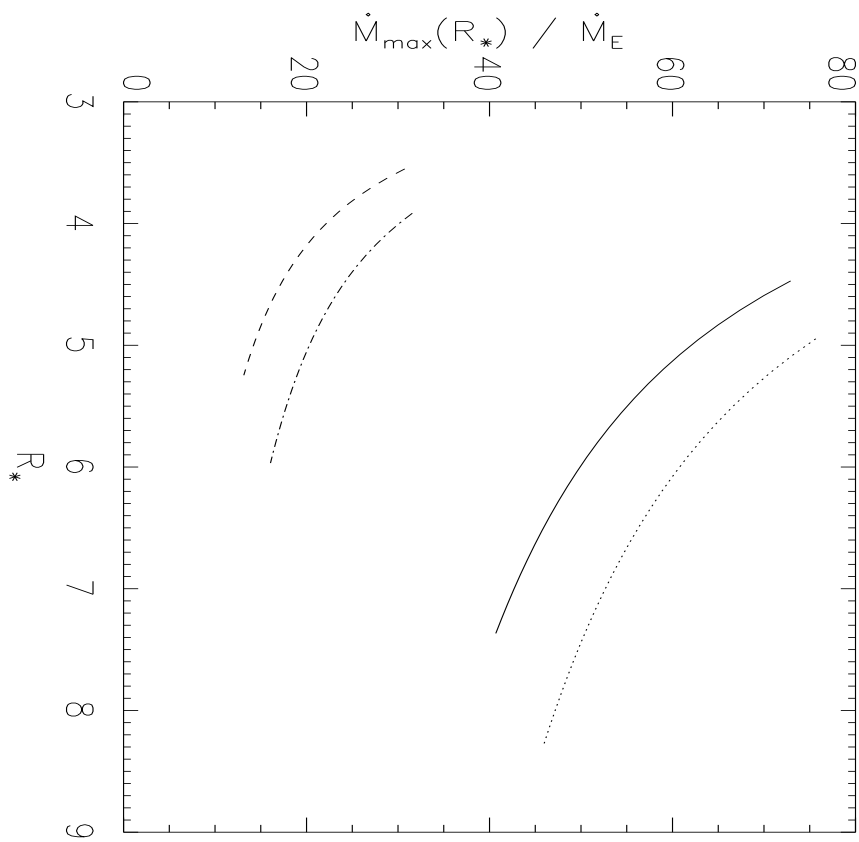


Figure 8: Upper limit on the accretion rate \dot{M}_{\max}/\dot{M}_E plotted as a function of R_* using eq. (6.10) for each of the models. For accretion rates exceeding \dot{M}_{\max} , losses due to strong proton-proton collisions in the corona overwhelm the shear acceleration.

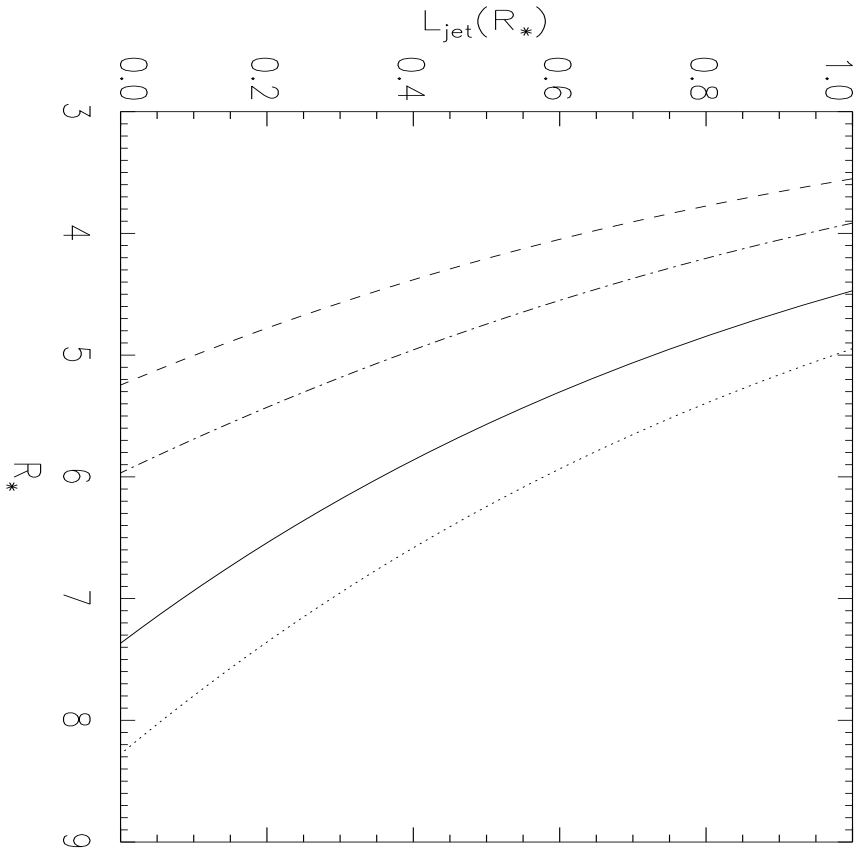


Figure 9: Asymptotic kinetic luminosity of the jet L_{jet} (eq. [6.16]) plotted in units of the maximum accretion luminosity $(1/2)\dot{M}_{\text{out}} c^2$ as a function of R_* . The inner radius of the jet, R_{in} , is defined as the radius at which this quantity reaches unity (see Table 1).

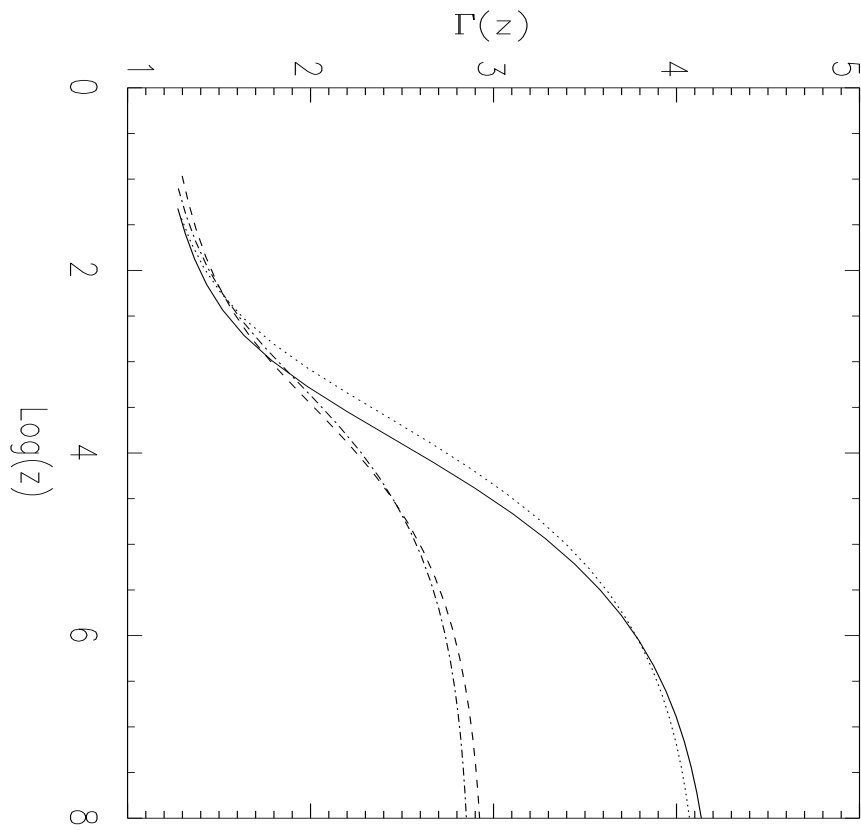


Figure 10: Lorentz factor Γ (eq. [5.7]) plotted as a function of the height z/R_g measured from the midplane of the disk for starting radius $R = R_{\text{out}}$. Note that the flow continues to accelerate at large distances from the black hole.

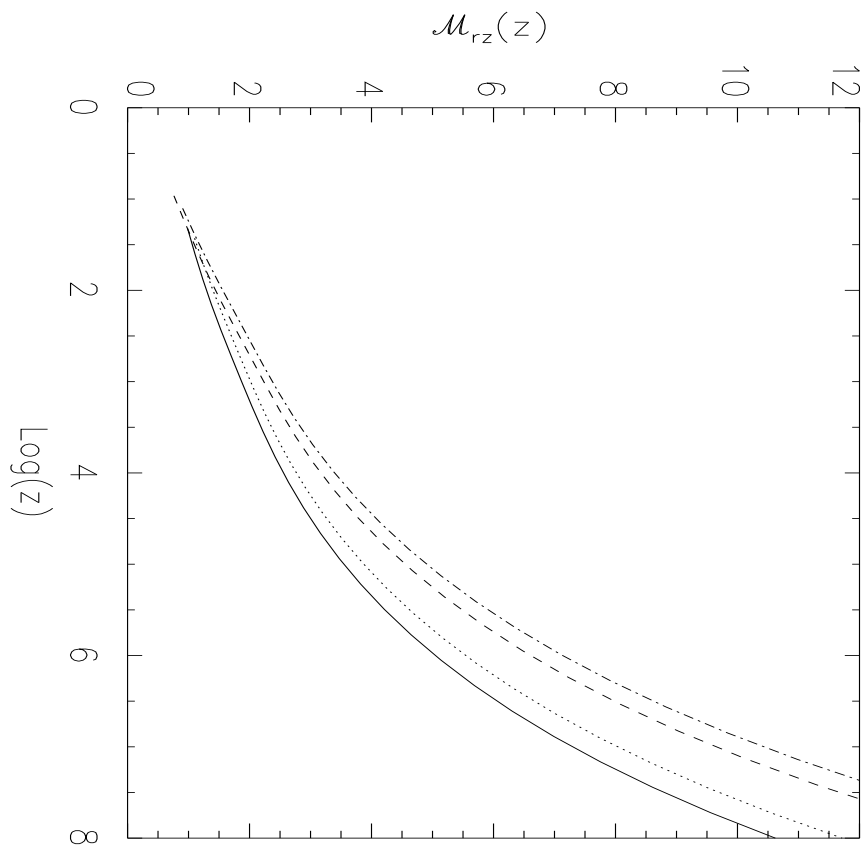


Figure 11: Mach number in the (r, z) plane, \mathcal{M}_{rz} , plotted as a function of the height z/R_g above the midplane of the disk using eq. (7.3) for starting radius $R = R_{\text{out}}$.

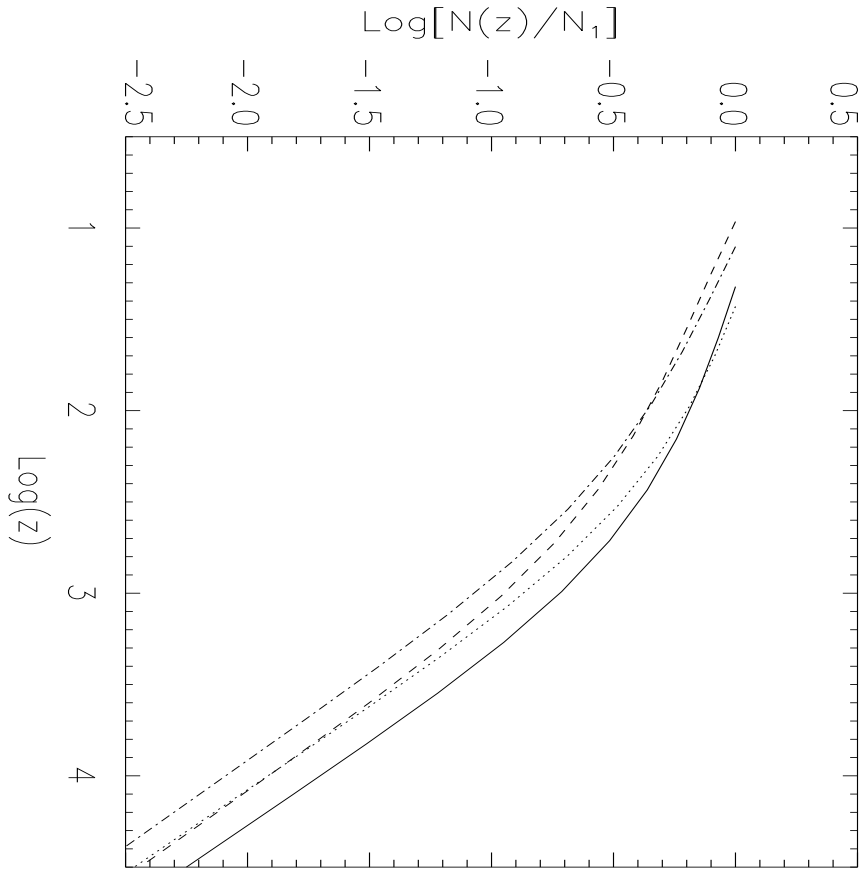


Figure 12: Variation of the number density in the wind N plotted as a function of the height z/R_g above the disk midplane for starting radius $R = R_{\text{out}}$.

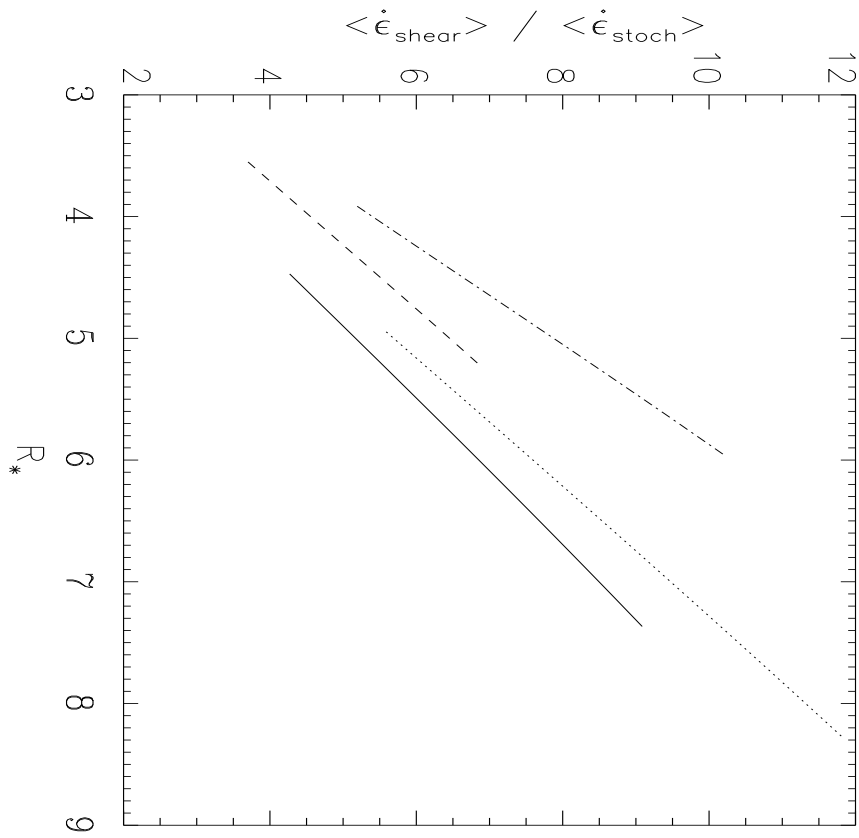


Figure 13: Ratio of the shear acceleration rate $\langle \dot{\epsilon}_{\text{shear}} \rangle$ to the stochastic acceleration rate $\langle \dot{\epsilon}_{\text{stoch}} \rangle$ plotted as a function of R_* , evaluated using eq. (8.8). Note that $\langle \dot{\epsilon}_{\text{shear}} \rangle$ greatly exceeds $\langle \dot{\epsilon}_{\text{stoch}} \rangle$ at all radii.